ADVANCED MATERIALS
www.advmat.de

Check for updates

Unveiling Charge-Transport Mechanisms in Electronic Devices Based on Defect-Engineered MoS_2 Covalent Networks

*Stefano Ippolito, Francesca Urban, Wenhao Zheng, Onofrio Mazzarisi, Cataldo Valentini, Adam G. Kelly, Sai Manoj Gali, Mischa Bonn, David Beljonne, Federico Corberi, Jonathan N. Coleman, Hai I. Wang, and Paolo Samorì**

Device performance of solution-processed 2D semiconductors in printed electronics has been limited so far by structural defects and high interflake junction resistance. Covalently interconnected networks of transition metal dichalcogenides potentially represent an efficient strategy to overcome both limitations simultaneously. Yet, the charge-transport properties in such systems have not been systematically researched. Here, the charge-transport mechanisms of printed devices based on covalent MoS_2 networks are unveiled via multiscale analysis, comparing the effects of aromatic versus aliphatic dithiolated linkers. Temperature-dependent electrical measurements reveal hopping as the dominant transport mechanism: aliphatic systems lead to 3D variable range hopping, unlike the nearest neighbor hopping observed for aromatic linkers. The novel analysis based on percolation theory attributes the superior performance of devices functionalized with π-conjugated molecules to the improved interflake electronic connectivity and formation of additional percolation paths, as further corroborated by density functional calculations. Valuable guidelines for harnessing the charge-transport properties in MoS_2 devices based on covalent networks are provided.

1. Introduction

The discovery and isolation of 2D materials (2DMs) represent veritable breakthroughs in materials science owing to their wide-ranging portfolio of electronic and optoelectronic properties,[1] paving the way for disruptive and exotic technologies such as More-than-Moore and Internet-of-Things devices.[2] In the past two decades, tremendous research efforts have been devoted to developing novel methods and strategies for the large-scale production of 2DMs, aiming for the best trade-off among quality, high throughput, and low cost.[3] Solution processing represents the most effective protocol to attain high-concentration and high-volume dispersions (also referred to as “inks”) of 2DMs; among them, liquid phase exfoliation is an efficient strategy to convert bulk layered materials into thin nanosheets dispersed in a suitable solvent.[4] These inks can be printed into thin films using several approaches, including inkjet printing, screen printing, and spray coating,[5] thereby promoting the advances of 2DM-printed electronics where low-cost and large-area fabrication is as relevant as device performance. In this regard, the ever-growing interest in 2D semiconductors for (opto)electronics has led to the great success of transition metal dichalcogenides (TMDs). Their extremely versatile physicochemical properties ensure a broad range of applicability, further expanded through ad hoc functionalization strategies using molecular chemistry approaches.[6–11] Nevertheless, progress is still hampered by structural defects, negatively

S. Ippolito, F. Urban, C. Valentini, P. Samorì
ISIS UMR 7006
Université de Strasbourg
CNRS
8 Allée Gaspard Monge, Strasbourg 67000, France
E-mail: samori@unistra.fr

W. Zheng, M. Bonn, H. I. Wang
Max Planck Institute for Polymer Research
Ackermannweg 10, 55128 Mainz, Germany

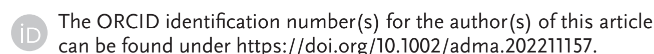
The ORCID identification number(s) for the author(s) of this article can be found under https://doi.org/10.1002/adma.202211157.

© 2023 The Authors. Advanced Materials published by Wiley-VCH GmbH. This is an open access article under the terms of the Creative Commons Attribution License, which permits use, distribution and reproduction in any medium, provided the original work is properly cited.

DOI: 10.1002/adma.202211157

O. Mazzarisi
Max Planck Institute for Mathematics in the Sciences
Inselstraße 22, 04103 Leipzig, Germany

A. G. Kelly, J. N. Coleman
School of Physics
Centre for Research on Adaptive Nanostructures
and Nanodevices (CRANN) and Advanced Materials
and Bioengineering Research (AMBER)
Trinity College Dublin
Dublin 2 D02 K8N4, Ireland

S. M. Gali, D. Beljonne
Laboratory for Chemistry of Novel Materials
Université de Mons
Place du Parc 20, 7000 Mons, Belgium

F. Corberi
Department of Physics
University of Salerno
Via Giovanni Paolo II 132, 84084 Fisciano (SA), Italy

15214095, 2023, 15, Downloaded from https://onlinelibrary.wiley.com/doi/10.1002/adma.202211157 by Cochrane France, Wiley Online Library on [13/04/2023]. See the Terms and Conditions (https://onlinelibrary.wiley.com/terms-and-conditions) on Wiley Online Library for rules of use; OA articles are governed by the applicable Creative Commons License

impacting their electronic properties and, thereby, device performance.[12] Furthermore, the poor interflake electronic connectivity (viz. high interflake electrical resistance) significantly impedes the charge carrier transport, constituting a major bottleneck in the development of TMD-printed (opto)electronics, especially in large-area and high-performance device applications.[13] Recently, we have devised an innovative molecular functionalization strategy to simultaneously overcome both limitations, by healing the most abundant structural defects in solution-processed TMDs (i.e., sulfur vacancies, V_S) and bridging adjacent flakes by using π-conjugated dithiolated molecules, thereby leading to the formation of covalently interconnected networks with enhanced electrical performance.[14] Although the charge-transport mechanisms in individual TMD nanosheets have already been meticulously studied,[15–17] very few similar studies have been performed on thin films.[18] More importantly, little is known about transport in TMD covalent networks, leaving a significant and crucial gap in our understanding. In this article, we unveil the charge-transport mechanisms in solution-processed covalent MoS_2 networks by investigating their temperature-dependent electrical conductivity. The MoS_2 ink, prepared by ultrasonication, is first deposited into ≈500 nm thick films via spray coating on bare or electrode-patterned Si/SiO_2 substrates. Then, the MoS_2 functionalization is performed under nitrogen-controlled atmosphere using a 50 mM solution of i) π-conjugated 1,4-benzenedithiol (BDT) or ii) aliphatic 1,3-propanedithiol (PDT) in anhydrous hexane, yielding the related covalent networks (Experimental Section). The in-depth multiscale investigation of covalent MoS_2 networks is reported elsewhere.[14] In a joint experimental and theoretical investigation, we prove that the charge transport in MoS_2 films and networks is dominated by interflake hopping, whose efficiency and detailed mechanism critically depend on the chemical structure of the linker.

2. Results and Discussion

2.1. Terahertz Spectral Analysis: MoS_2 Films and Networks

To shed light on the electrical transport properties of MoS_2 films and covalent networks, we exploit optical-pump terahertz (THz)-probe spectroscopy. Due to the transient nature of THz pulses, charge carriers are locally driven over a short distance (approximately tens of nanometers), mainly probing the intraflake transport properties[19–21] and complementing the measurements performed on electrical devices, where both intra- and interflake contributions occur. As displayed in the schematic of **Figure 1**a, optical excitation (i.e., laser pulses with a duration of ≈50 fs and photon energy of 3.10 eV) injects charge carriers in MoS_2 samples, whose photoconductivity ($\Delta\sigma_{ph}$) is sequentially probed by a single cycle THz pulse (with a peak electric field equal to E). The $\Delta\sigma_{ph}$ can be extrapolated from the photoinduced THz absorption following $\Delta\sigma_{ph} \propto -\Delta E/E$ (with

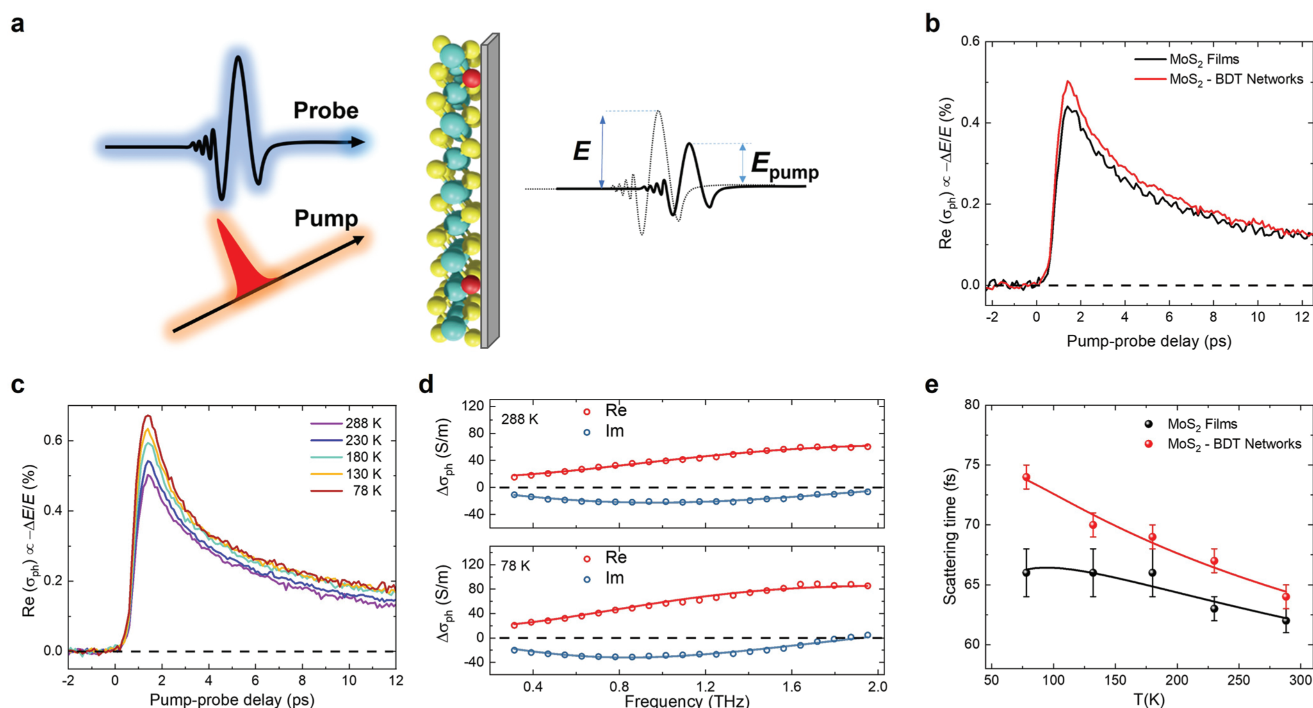

Figure 1. THz spectral analysis on MoS_2 films and covalent networks. a) Schematic illustration of optical-pump–THz-probe spectroscopy on MoS_2 systems. b) Photoconductivity dynamics of pristine MoS_2 films and MoS_2–BDT networks (absorbed photon density ≈10^{17} m^{-2}). c) Photoconductivity dynamics of MoS_2–BDT networks within the T range 288–78 K under vacuum conditions (≈10^{-4} mbar). d) Complex photoconductivity spectra for MoS_2–BDT networks at 288 and 78 K, recorded ≈2 ps after photoexcitation (red circles: real photoconductivity; blue circles: imaginary photoconductivity). The solid lines represent the data fitting using the Drude–Smith model. e) Scattering time as a function of T for pristine MoS_2 films and MoS_2–BDT networks. The solid lines in (e) show a simple model (Experimental Section) for electron–phonon coupling (identical for both systems) and impurity scattering (enhanced for MoS_2 films).

 © 2023 The Authors. Advanced Materials published by Wiley-VCH GmbH

15214095, 2023, 15, Downloaded from https://onlinelibrary.wiley.com/doi/10.1002/adma.202211157 by Cochrane France, Wiley Online Library on [13/04/2023]. See the Terms and Conditions (https://onlinelibrary.wiley.com/terms-and-conditions) on Wiley Online Library for rules of use; OA articles are governed by the applicable Creative Commons License

$\Delta E = E_{pump} - E$, where E_{pump} represents the transmitted THz field from the sample with photoexcitation).[19] We find that $\Delta\sigma_{ph}$ of MoS_2–BDT networks increases by ≈10% compared to pristine MoS_2 films (Figure 1b), and a similar enhancement factor of $\Delta\sigma_{ph}$ is recorded for MoS_2–PDT networks as well (Section S2, Supporting Information). Such observations support the passivation of V_S by BDT and PDT molecules (viz., decreasing the overall defect density) and thus the resulting increase of $\Delta\sigma_{ph}$, regardless of the chemical structure of the linkers, i.e., aromatic versus aliphatic. To further investigate the intraflake charge-transport properties in MoS_2 films and networks, as well as to disentangle its contribution from the overall conductivity in electrical devices, we conduct temperature (T)-dependent $\Delta\sigma_{ph}$ measurements.

Figure 1c shows that $\Delta\sigma_{ph}$ of MoS_2–BDT networks increases upon lowering the temperature from 288 to 78 K. Such a behavior is typical for band-like transport, with charge carrier mobility within MoS_2 flakes limited by the carrier–phonon scattering.

The Drude–Smith model (Experimental Section), widely used to explain charge transport in nanomaterials,[19,22,23] well describes and fits our experimental data (Figure 1d). The inferred T-dependent charge scattering times for pristine MoS_2 films and MoS_2–BDT networks are displayed in Figure 1e.

The charge scattering time in both MoS_2 films and MoS_2–BDT networks increases with decreasing T, in agreement with phonon-scattering-limited band-like transport within MoS_2 flakes. Moreover, we analyze the T-dependent scattering time assuming contributions from phonon and impurity scatterings (Experimental Section). This data analysis reveals an ≈40% decrease in the carrier–defect scattering rate for MoS_2–BDT networks compared with pristine MoS_2 films, demonstrating the positive effect of the thiol group on the healing of V_S.

MoS_2 electrical devices show a thermally activated charge carrier transport and an increase of the device figures of merit by one order of magnitude upon BDT functionalization.[14]

Thus, the modest transport enhancement recorded for the intraflake contribution via THz analysis (≈10% at room temperature) provides unambiguous evidence that the performance in MoS_2 electrical devices is dominated by interflake transport, whose mechanisms are discussed below.

2.2. Charge Carrier Transport: Hopping Mechanisms in MoS_2 Devices

Charge carrier transport in polycrystalline, highly disordered, and defective materials is generally governed by hopping between localized defective states.[24–27] To shed light on the charge-transport mechanisms involved in MoS_2 films and networks (**Figure 2**a), we investigate their T-dependent electrical conductivity (σ). To this end, we carry out two-point probe measurements and assess the electrical device performance from 340 to 5 K (Figure 2b). The maximum σ for MoS_2–PDT networks is higher than pristine films by a factor 3 ± 1, confirming our previously reported data and highlighting the effects of thiolated systems on the healing of V_S in TMDs.[14] Conversely, the network formation with aromatic BDT molecules increases σ by one order of magnitude.

As shown in the inset of Figure 2b, two different regimes can be recognized in the σ versus T plots: i) a thermally activated regime (hopping regime), in the T range 340–200 K, with an exponential dependence of σ on T; ii) a T-independent behavior (tunneling regime) between 150 and 5 K.[28] In the transition region (200–150 K), tunneling and hopping regimes occur simultaneously.[29]

In the tunneling regime, the functionalization of pristine MoS_2 films with dithiolated molecules does not affect the $\sigma(T)$ curves, unlike significant variations observed in the hopping region. We identify the hopping mechanisms by extracting the exponent α from the data, with $\alpha \le 1$, using the equation

$$\sigma(T) = \sigma_0 \exp\left[-\left(\frac{T_0}{T}\right)^{\alpha}\right] = \frac{1}{\rho(T)} \tag{1}$$

with σ_0, T_0, and ρ representing the prefactor, characteristic temperature, and resistivity of the system, respectively. For $\alpha = 1$, $\sigma(T)$ is proportional to $\exp(E_a/k_B T)$, where $E_a = k_B T_0$ defines the activation energy of the nearest neighbor hopping (NNH) mechanism,[24,25] which involves the hop of the charge carrier between the two spatially nearest trap sites, despite their energy levels. On the contrary, all variable range hopping (VRH) mechanisms display $\alpha < 1$, and the transport is ruled by charge carrier hopping between the two most energetically favorable sites, regardless of their spatial distance.[30,31]

In particular, the Mott-VRH mechanisms exhibit $\alpha = 1/(1+d)$, where d is the dimensionality of the system (e.g., $\alpha = 1/4$ for 3D Mott VRH). A different mechanism known as Efros–Shklovskii VRH (ES-VRH) arises for $\alpha = 1/2$, where a Coulomb gap is opened in the density of states (DOS) at the Fermi level, and the hopping transport is strongly affected by Coulomb scattering of the charge carriers with charged centers.[32,33] Thus, we extract α to reveal the interflake hopping mechanisms involved in each of our systems. We first calculate the reduced activation energy (W)

$$W = -\frac{T}{\rho}\frac{d\rho}{dT} \tag{2}$$

Upon linearization of Equation (2), the slope of ln(W) versus ln(T) plot returns α. The three systems under investigation show distinct hopping mechanisms (Figure 2c). Pristine MoS_2 films exhibit $\alpha = 1/2$, indicating an ES-VRH mechanism governed by the scattering of the charge carriers with fixed charged centers. For MoS_2–PDT networks and MoS_2–BDT networks, we extract $\alpha = 1/4$ and $\alpha = 1$, respectively. The aliphatic PDT molecules, upon healing of V_S, neutralize the Coulombic scattering centers involved in the hopping mechanism of pristine MoS_2 films and, thus, lead to a transition from ES-VRH to 3D Mott VRH.[15,16,18,34,35] A transition to the hopping mechanism is also recorded for the functionalization with π-conjugated BDT molecules, where we observe a change from ES-VRH, characteristic of pristine MoS_2 films, to NNH mechanism. The aromatic ring enhances the interflake transport by bridging two adjacent flakes and improving their electronic connectivity, thereby creating favorable conduction paths for the charge carriers, as supported by the theoretical calculations reported below.

Furthermore, we extrapolate the average hopping distance (R_{hop}) for the three systems by using the characteristic

 © 2023 The Authors. Advanced Materials published by Wiley-VCH GmbH

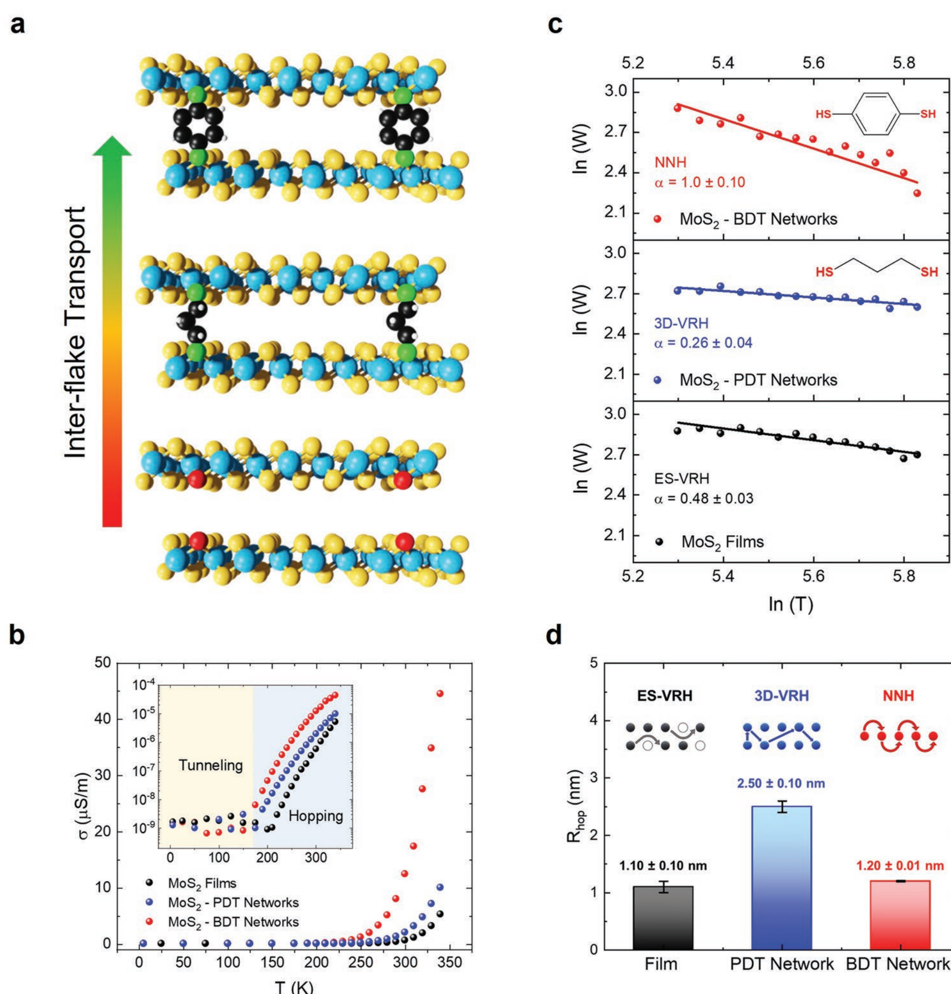

Figure 2. Charge-transport analysis in printed MoS_2 devices. a) Sketch of V_S healing mechanism and network formation in pristine MoS_2 films by aliphatic PDT and aromatic BDT molecules, highlighting the effects on the interflake charge transport. Atom color legend: sulfur (yellow), molybdenum (light blue), sulfur vacancy (red), sulfur healing (green), carbon (black), hydrogen (light gray). b) σ versus T plots for MoS_2 films, MoS_2–PDT networks, and MoS_2–BDT networks. Inset: σ versus T curves displayed on a logarithmic scale. All curves are recorded with $V = 10$ V. c) ln(W) versus ln(T) plots for MoS_2 films, MoS_2–PDT networks, and MoS_2–BDT networks. All α values are extracted at $V = 1$ V. d) Extrapolated R_{hop} for MoS_2 films, MoS_2–PDT networks, and MoS_2–BDT networks, along with a sketch of their hopping mechanisms.

equations related to each hopping mechanism (Experimental Section). A sketch of the hopping mechanisms as well as the extrapolated R_{hop} for the systems under investigation are displayed in Figure 2d. The increase in R_{hop} moving from pristine MoS_2 films ($R_{ES\text{-}VRH} = 1.10 \pm 0.10$ nm) to MoS_2–PDT networks ($R_{3D\text{-}VRH} = 2.50 \pm 0.10$ nm) is ascribed to the healing of V_S and, thus, the decrease of the overall defect density. The R_{hop} for MoS_2–BDT networks $R_{NNH} = 1.20 \pm 0.01$ nm points to different and additional effects upon healing of V_S and network formation. In fact, MoS_2 networks produced with π-conjugated BDT linkers benefit from an exclusive enhanced interflake electronic connectivity (i.e., reduced interflake resistance), promoting enhanced hopping transport through adjacent flakes. Comparing the R_{hop} for MoS_2–PDT ($R_{3D\text{-}VRH} = 2.50 \pm 0.10$ nm) and MoS_2–BDT networks ($R_{NNH} = 1.20 \pm 0.01$ nm), the latter value suggests that the hop of a charge carrier occurs from a hopping site to the spatially closest one through the BDT bridging molecule, whose length is ≈0.7 nm.

2.3. Density Functional Theory (DFT) Calculations of Covalent MoS_2 Networks

To understand the role of dithiolated molecules during the healing of V_S and network formation, as well as related effects on the interflake charge transport, DFT calculations are performed on bulk pristine MoS_2 crystals, bulk defective MoS_2 crystals (with V_S), MoS_2–BDT, and MoS_2–PDT networks. The MoS_2 crystal structure we consider for this study contains one layer per unit cell, where the interflake stacking (along the *c*-axis) replicates the AA stacking mode.[36]

Starting from the pristine MoS_2 crystals with one layer per unit cell (**Figure 3**a), V_S are created by removing two sulfur atoms (referred to as MoS_2–$2V_S$) either directly on top of each other or diagonally to each other (Section S4, Supporting Information), such that the V_S concentration is kept at 6% in both cases, consistent with previous reports.[37,38] Of such two configurations, the latter is found to be energetically more

 © 2023 The Authors. Advanced Materials published by Wiley-VCH GmbH

15214095, 2023, 15, Downloaded from https://onlinelibrary.wiley.com/doi/10.1002/adma.202211157 by Cochrane France, Wiley Online Library on [13/04/2023]. See the Terms and Conditions (https://onlinelibrary.wiley.com/terms-and-conditions) on Wiley Online Library for rules of use; OA articles are governed by the applicable Creative Commons License

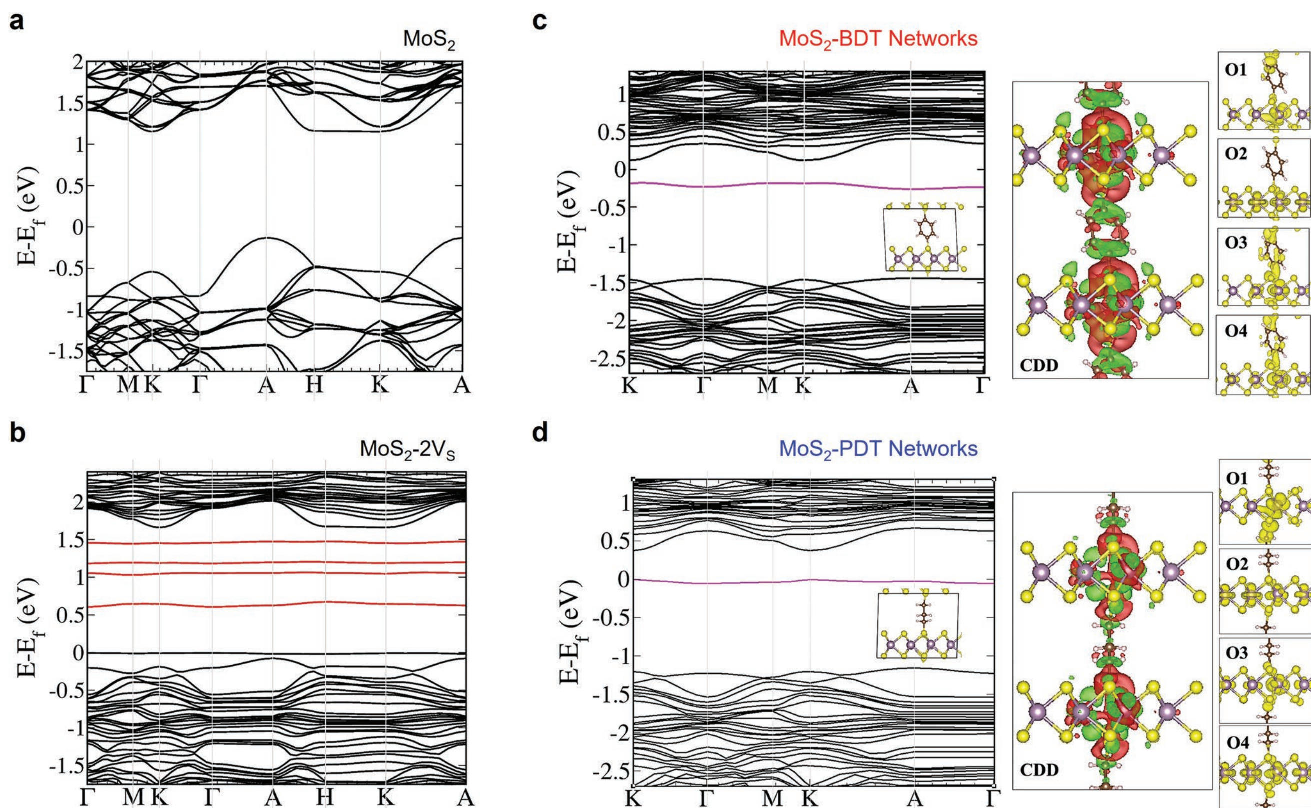

Figure 3. DFT calculations for MoS_2 films and covalent networks. a,b) Electronic band structure of bulk MoS_2 crystal in its pristine (a) and defective (b) form (MoS_2–$2V_S$, with 6% V_S). c,d) Electronic band structure of MoS_2–BDT (c) and MoS_2–PDT (d) covalent networks (left panel). CDD plots (central panel) and crystalline orbitals (right panel) are also displayed. O1, O2, and O4 represent the crystalline orbitals (obtained at the *K*-point) of the occupied mid-gap state, the lowest unoccupied electronic state (LUCO, i.e., CBE), and the electronic state immediately following the CBE (LUCO + 1), respectively. O3 represents the LUCO in the middle of *K*–*A* path.

favorable by ≈20 meV per fractional unit when compared to the former, presenting defect states spread through the electronic bandgap (Figure 3b) which act as scattering centers and, thus, diminish the electron mobility.[39,40] When the structural defects are exposed to BDT and PDT molecules, the localized empty mid-gap defect states disappear, thereby restoring the electronic structure of pristine MoS_2 crystals. We also note that occupied mid-gap states appear within the electronic bandgap, as indicated by the magenta curves in Figure 3c,d.

When a BDT molecule is used to connect two MoS_2–$2V_S$ surfaces (Figure 3c, left panel), these mid-gap states are delocalized both on the BDT molecule and the underlying MoS_2–$2V_S$ surfaces, indicating a strong hybridization for such a dyad. The charge density difference (CDD) plots (Figure 3c, central panel) also display a strong delocalization of the electron density through the bridging BDT molecule connecting the two MoS_2–$2V_S$ flakes. Most importantly, such a strong hybridization between BDT molecules and MoS_2–$2V_S$ surfaces is also observed in the crystalline orbitals around the conduction band edge (CBE) (Figure 3c, right panel). On the contrary, in the case of PDT molecules (Figure 3d, left panel), the electron density from the two MoS_2–$2V_S$ surfaces through the aliphatic molecule hardly extends (Figure 3d, central panel), and the crystalline orbitals around the CBE do not show any significant contribution from the PDT molecule (Figure 3d, right panel). The electronic structure of MoS_2–BDT networks as well as their CDD and orbital plots provide an unambiguous indication that π-conjugated BDT molecules not only heal the localized mid-gap defect states due to V_S but also bridge two adjacent MoS_2–$2V_S$ flakes, improving their interflake electronic connectivity. Conversely, aliphatic PDT molecules do not provide a similar enhancement, as they solely induce the healing of localized mid-gap defect states and the recovery of the electronic structure of pristine MoS_2 crystals.

Moreover, we calculate the electron effective mass (m^*) at the CBE for the three systems under investigation. Remarkably, the m^* in MoS_2–BDT networks is significantly lower than MoS_2–$2V_S$ and MoS_2–PDT networks, being comparable to that of pristine MoS_2 crystals and highlighting an enhanced interflake electronic connectivity and charge transport (Table S4, Supporting Information).

2.4. Covalent MoS_2 Networks for Flexible Electronic Applications

For our electrical characterization, thin-film transistors (TFTs) are produced by spray coating MoS_2 films onto prepatterned substrates with interdigitated gold electrodes (Au-IDEs, serving as source and drain electrodes) and coplanar gate configuration. All steps related to the device fabrication, deposition,

 © 2023 The Authors. Advanced Materials published by Wiley-VCH GmbH

15214095, 2023, 15, Downloaded from https://onlinelibrary.wiley.com/doi/10.1002/adma.202211157 by Cochrane France, Wiley Online Library on [13/04/2023]. See the Terms and Conditions (https://onlinelibrary.wiley.com/terms-and-conditions) on Wiley Online Library for rules of use; OA articles are governed by the applicable Creative Commons License

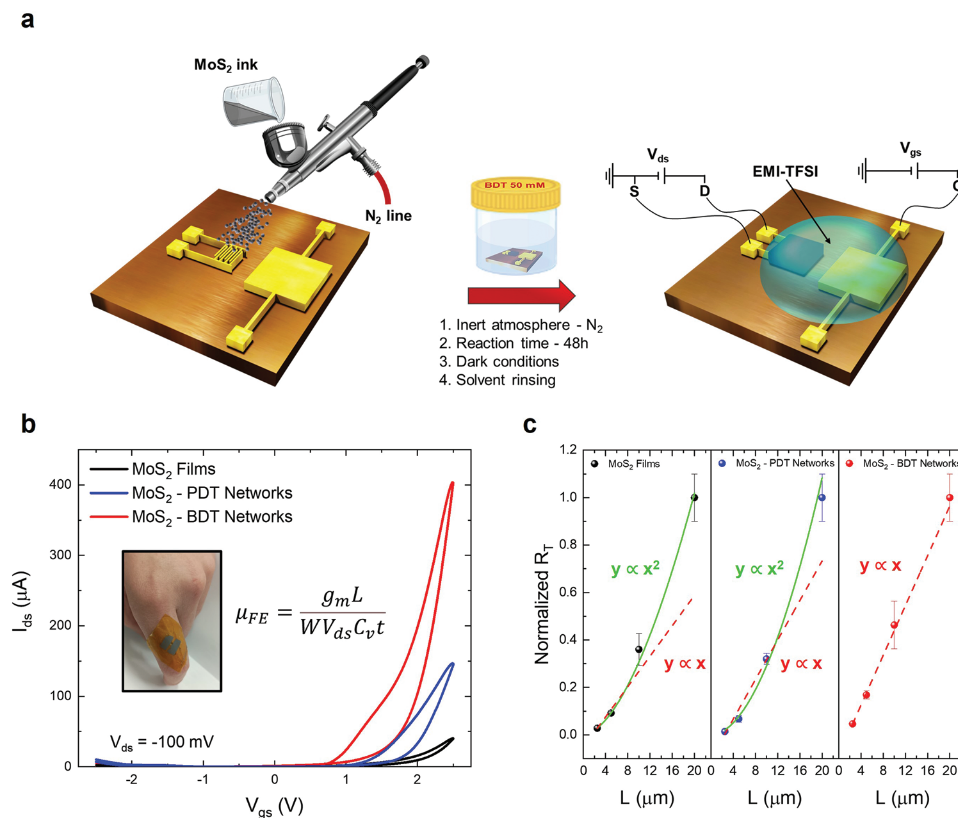

Figure 4. Electrical characterization of printed MoS_2 devices. a) Cartoon of MoS_2 deposition, functionalization, and electrical characterization. b) Transfer characteristics for MoS_2 films, MoS_2–PDT networks, and MoS_2–BDT networks, recorded using EMI–TFSI as electrolyte gate. Inset: printed TFT device on PI flexible substrate. c) Normalized R_T versus L plots for MoS_2 films, MoS_2–PDT networks, and MoS_2–BDT networks, based on their TLM analysis performed in two-point probe configuration. R_T is calculated at 10 V for all systems. In the experimental data, the allometric and linear fits are displayed for MoS_2 films (left), MoS_2–PDT networks (middlel), and MoS_2–BDT networks (right).

and functionalization procedures are proved to be compatible with both rigid (Si/SiO_2) and flexible polyimide (PI) substrates (Kapton tape), supporting the progress of printed devices in flexible electronics (**Figure** 4a).

It is known that dielectric-gated TFTs based on solution-processed TMDs exhibit poor current switching ($I_{ON}/I_{OFF} < 10$),[41] encouraging the use of an electrolyte solution that modulates the device volumetrically.[14,42,43] In our devices, MoS_2 films and networks are gated by 1-ethyl-3-methylimidazolium bis(trifluoromethylsulfonyl) imide (EMI–TFSI) ionic liquid (IL), where the application of a gate voltage (V_{gs}) induces the formation of an electrical double layer at the IL/MoS_2 interface and results in a strong current modulation.[14,42,43] The typical transfer curves for pristine MoS_2 films, MoS_2–BDT networks, and MoS_2–PDT networks, recorded on PI substrates, are displayed in Figure 4b. As previously reported,[14] the electrical characteristics of TFTs based on MoS_2–BDT networks outperform those of pristine MoS_2 films and MoS_2–PDT networks, exhibiting an increase by one order of magnitude in the main device figures of merit. In particular, MoS_2–BDT networks reach field-effect mobilities and I_{ON}/I_{OFF} ratios up to 10^{-2} cm^2 V^{-1} s^{-1} and to 10^4, respectively (Table S5, Supporting Information), as a result of the improved interflake electronic connectivity.

For both MoS_2 film and network devices (in dry state, i.e., absence of IL), we take advantage of the transfer length method (TLM) to extrapolate the contact resistance (Section S5, Supporting Information) and assess its influence on the total device resistance (R_T). To this end, we fabricate Au-IDEs with four different channel lengths (L) and investigate the R_T versus L behavior for the three systems under analysis, deriving R_T from their characteristic I–V curves. From TLM on pristine MoS_2 films (Figure 4c, left panel), our experimental data do not comply with the theoretical linear behavior of the R_T versus L (red curve), showing a quadratic dependence on L (green curve) instead, thereby highlighting a $1/L$ trend for σ. An identical behavior is observed upon using aliphatic linkers, with MoS_2–PDT networks showing a similar trend to pristine MoS_2 films (Figure 4c, central panel). Notably, MoS_2–BDT networks exhibit the ideal linear dependence of R_T on L (Figure 4c, right panel), owing to the improved interflake electronic connectivity upon dithiol functionalization.

Printed devices based on solution-processed TMDs represent highly porous aggregates of 2D rigid nanosheets, where morphological imaging by electron microscopy reveals a limited area of physical overlap among adjacent flakes, thereby yielding a high junction resistance and hindering the overall charge carrier transport.[13] The morphology, structural disorder, and defective nature of our multiflake systems are responsible for the dominant interflake resistance, where the physical and electronic connectivity among nanosheets defines a percolative pattern in-between the electrodes.

© 2023 The Authors. Advanced Materials published by Wiley-VCH GmbH

15214095, 2023, 15, Downloaded from https://onlinelibrary.wiley.com/doi/10.1002/adma.202211157 by Cochrane France, Wiley Online Library on [13/04/2023]. See the Terms and Conditions (https://onlinelibrary.wiley.com/terms-and-conditions) on Wiley Online Library for rules of use; OA articles are governed by the applicable Creative Commons License

15214095, 2023, 15, Downloaded from https://onlinelibrary.wiley.com/doi/10.1002/adma.202211157 by Cochrane France, Wiley Online Library on [13/04/2023]. See the Terms and Conditions (https://onlinelibrary.wiley.com/terms-and-conditions) on Wiley Online Library for rules of use; OA articles are governed by the applicable Creative Commons License

2.5. Percolation Theory: Random Resistor Networks

The abovementioned anomalous dependence of σ on L is due to the percolation process occurring within the channels of our electrical devices, and it can be discussed and rationalized within the framework of random resistor networks.[44,45] The channel can be modeled as a 2D random resistor network, where the probability to find a bond (i.e., resistor of the percolation path) is given by p (**Figure 5**a).

Here, the effective conductivity (σ_{eff}) at criticality (i.e., percolation threshold $p = p_c$) scales as

$$\sigma_{\mathrm{eff}}(L) \sim L^{-\beta} \tag{3}$$

with $\beta = 0.95 \pm 0.01$.[44] Slightly above criticality, σ_{eff} is expected to follow the critical behavior for short enough L, reaching then a constant value proportional to $(p - p_c)^t$, with $t \cong 1.28$.[44] Figure 5b shows the normalized σ values $[\sigma(L)/\sigma(2.5\ \mu\mathrm{m})]$ as a function of L for our three systems. The curves related to MoS_2 films and MoS_2–PDT networks collapse (i.e., overlap), proving that PDT exposure merely improves the already existing percolation paths (i.e., bonds) due to the healing of V_S, mainly located at the flake edges.[14] On the other hand, a distinct feature is unique to MoS_2–BDT networks: the different σ saturation level at long channels clearly indicates an additional benefit due to the network formation, which is ascribed to the creation of additional percolation paths as a result of the improved inter-flake electronic connectivity upon using π-conjugated linkers.

To investigate the role of additional percolation paths resulting from the network formation, we explore the influence of the concentration of functionalizing molecule (c_M) on the σ versus L dependence at three different c_M. We find a clear σ enhancement proportional to BDT c_M; in particular, upon increasing the c_M from 500 µm to 50 mm, the saturation level changes by ≈100% because of the generation of new percolation paths within the channel (Figure 5c). Considering $\sigma_{\mathrm{eff}} \equiv \sigma(L, c_M)$, it can be written

$$\sigma_k(L, c_M) = A_k(c_M)\left\{\left[p_k(c_M) - p_c\right]^t + bL^{-\beta}\right\} \tag{4}$$

where $A_k(c_M)$ represents the average conductivity of a single bond, the index k refers to different devices, and b denotes the coefficient regulating the size dependence of σ in the percolation problem, which only depends on geometrical features. We claim, therefore, that the latter quantity does not significantly depend on c_M nor on k.

As reported in the Experimental Section, we can use the following approximate expression to describe the experimental data, defining the ratio $r_{k,k}(L,c_M,0)$ between $\sigma_k(L,c_M)$ of MoS_2 samples before and after BDT functionalization

$$r_{k,k}(L, c_M, 0) \simeq a_{k,k}(c_M, 0)\frac{\left[p_k(c_M) - p_c\right]^t + bL^{-\beta}}{bL^{-\beta}} \tag{5}$$

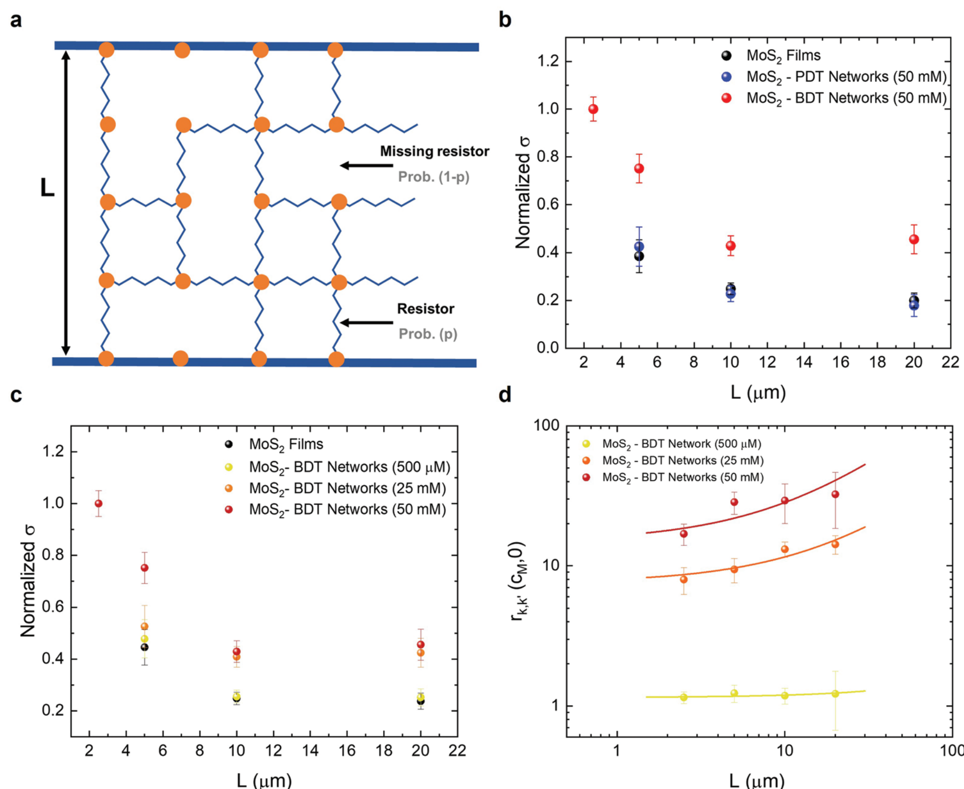

Figure 5. Percolation theory in MoS_2 films and covalent networks. a) Sketch of the random resistor network model, where p and $1 - p$ represent the probability of a resistor and missing resistor, respectively. b) Normalized σ versus L plot showing the critical $1/L$ trend for MoS_2 films and 50 mm-functionalized MoS_2–PDT and MoS_2–BDT networks. The normalized σ values at $L = 2.5$ µm coincide for all systems. c) Normalized σ versus L plot for MoS_2–BDT networks as a function of BDT concentration, ranging from 500 µm to 50 mm. The normalized σ values at $L = 2.5$ µm coincide for all systems. d) $r_{k,k'}(c_M,0)$ versus L curves for MoS_2–BDT networks at three different values of c_M. The dots (with error bars) represent the experimental data, while the continuous lines are the analytic form Equation (5) with the fitted parameters $a_{k,k}(c_M,0)$ and $p_k(c_M) - p_c$.

© 2023 The Authors. Advanced Materials published by Wiley-VCH GmbH

15214095, 2023, 15, Downloaded from https://onlinelibrary.wiley.com/doi/10.1002/adma.202211157 by Cochrane France, Wiley Online Library on [13/04/2023]. See the Terms and Conditions (https://onlinelibrary.wiley.com/terms-and-conditions) on Wiley Online Library for rules of use; OA articles are governed by the applicable Creative Commons License

where $a_{k,k}(c_M,0) := A_k(c_M)/A_k(0)$ and with $b = 5.40\ \mu m^{\beta}$. The experimental determination of $r_{k,k'}(L,c_M,0)$ for three different values of c_M and the related analytic expressions are reported in Figure 5d. The two quantities $a_{k,k}(c_M,0)$ and $p_k(c_M) - p_c$ are obtained by best fit procedure where the data are proportionally weighted to their inverse squared experimental error. The results of the fitted parameters are shown in Table S8 (Supporting Information).

Figure 5d unambiguously demonstrates two different effects resulting from the BDT functionalization: i) the drastic increase of $a_{k,k}(c_M,0)$ with increasing c_M (highlighted by the overall value of $r_{k,k'}(c_M,0)$), pointing out an improved bond conductivity; ii) the increase of $p(c_M) - p_c$ (associated with the upward bending of $r_{k,k'}(c_M,0)$ vs L curves), revealing the formation of additional bonds due to the improved interflake electronic connectivity. Both effects contribute to increasing the overall $\sigma(L, c_M)$.

3. Conclusions

Our multiscale investigation on the transport properties of covalent MoS_2 networks reveals hopping as the dominant charge-transport mechanism, unveiling the paramount role played by the chemical structure of the bridging linkers. The improved interflake electronic connectivity, exclusively provided by π-conjugated BDT linkers, is pointed out in the TLM analysis, where a quadratic dependence in the R_T versus L plots is observed for pristine MoS_2 films and MoS_2–PDT networks, unlike the ideal linear trend restored in MoS_2–BDT networks due to the successful bridging of adjacent flakes. Furthermore, in agreement with DFT calculations, our innovative percolation analysis, conducted for the first time on MoS_2 electrical devices, confirms the improvement of already existing percolation paths and the formation of additional ones in MoS_2–BDT networks. In conclusion, we provide an analytical protocol to elucidate the charge transport in TMD devices. Moreover, our findings reveal that the defect engineering using suitably designed dithiolated molecules represents a powerful strategy for harnessing the transport properties in covalent MoS_2 networks, paving the way to the fabrication of high-performance devices for printed electronics.

4. Experimental Section

MoS_2 Ink Preparation: MoS_2 inks were obtained by sonicating the respective powders in *N*-methyl-2-pyrrolidone (NMP). An initial concentration of 20 mg mL^{-1} was processed for 1 h in 80 mL of NMP using a tip horn sonicator (Sonics Vibra-cell VCX-750 ultrasonic processor) at 60% amplitude. The resulting dispersion was centrifuged at 3218*g* for 1 h using a Hettich Mickro 220R, after which the supernatant was discarded to remove potential contaminants from the starting powder. The sediment was then redispersed in fresh NMP and sonicated under the same conditions for 6 h. This process gave a polydisperse stock dispersion from which flakes could be size selected by centrifugation. For each material, the polydisperse stock was first centrifuged at 106.4*g* for 90 min to remove the largest aggregates, with the sediment retained for future exfoliation. The supernatant was then centrifuged at 425*g* for 90 min to separate the smaller flakes. Finally, this sediment was redispersed in 30 mL of 2-propanol.

MoS_2 Ink Characterization: The as-exfoliated MoS_2 flakes, both in solution and solid state, were characterized by spectroscopic and morphological analysis. Detailed information was reported below.

MoS_2 Ink Characterization—UV–Vis Spectroscopy: UV–vis spectra were recorded under ambient conditions on a Perkin Elmer 1050 spectrometer equipped with an integrating sphere (150 mm) attachment, using quartz cuvettes with an optical path length of 4 mm. The concentration of the MoS_2 ink could be extracted from the UV–vis spectra by means of the Lambert–Beer law, using the extinction coefficient at 345 nm (69 mL mg^{-1} cm^{-1}) where it was relatively invariant across the lateral size and thickness of MoS_2 flakes.[46]

MoS_2 Ink Characterization—Raman Spectroscopy: Raman spectra were recorded under ambient conditions with a Renishaw inVia spectrometer at 532 nm with a 100× objective (numerical aperture 0.85). The power was kept below 1 mW to avoid local heating and damage effects.

MoS_2 Ink Characterization—Scanning Electron Microscopy (SEM): SEM images were captured using a Zeiss Ultra Plus, operating with a gun pressure ≈10^{-8} mbar and chamber pressure ≈10^{-6} mbar, working at 2–5 kV.

MoS_2 Ink Characterization—Atomic Force Microscopy (AFM): AFM images were taken with a Bruker Dimension Icon microscope under ambient conditions, operating in tapping mode and using TESPA-V2 tips with spring constant k = 42 N m^{-1}. The images were captured at a scan rate equal to 1.0 Hz with 1024 lines per image.

Electrical Device Fabrication: The source, drain, and gate electrodes of the device were patterned by photolithography (AZ1505 photoresist and MIF326 developer, MicroChemicals) using Microtech LW405B laser writer. 5 nm of chromium and 40 nm of gold were thermally evaporated with Plassys MEB 300, followed by liftoff in warm (50 °C) acetone for 90 min to output the final electrodes. Finally, the devices were rinsed with acetone and 2-propanol to remove photoresist residues. The device geometry displayed 22 interdigitated electrodes having channel lengths from 2.5 to 20 µm and channel width of 10 000 µm, while the area of the coplanar gate electrode was ≈1 mm^2. The very same protocol was used for both rigid (Si/SiO_2) and flexible (polyimide) substrates.

MoS_2 Ink Deposition: Before deposition, the electrode-patterned Si/SiO_2 substrates (1.5 × 1.5 cm^2) were cleaned by ultrasonication in acetone and 2-propanol for 10 min, each. Subsequently, they were heated on a hot plate at 80 °C, with their electrodes covered by blue masking tape. Then, 10 mL of MoS_2 ink (concentration ≈0.2 mg mL^{-1}) was sprayed on the substrate using a commercial airbrush gun (Timbertech ABPST01), with needle and nozzle diameter equal to 0.3 mm, supplied by compressed nitrogen at 1 bar. The distance between the nozzle tip and the substrate was kept at ≈20 cm.

Stylus Profilometry: The thickness of MoS_2 films was measured with a KLA-Tencor Alpha-Step IQ profilometer, operating under ambient conditions. All films showed a thickness of 500 ± 50 nm.

Functionalization Reaction: Upon deposition, the MoS_2 thin films were moved under N_2-controlled atmosphere (i.e., glovebox) for the following functionalization steps: i) sample immersion within BDT/PDT 50 mM solution in anhydrous hexane for 48 h (dark) inside a sealed container, ii) spin-rinsing with anhydrous hexane (5 mL, 4000 rpm, acceleration 4000 rpm s^{-1}, 60 s), and iii) spin-drying at the very same conditions. The preparation of BDT and PDT solutions (e.g., powder weighing, dissolution) was carried out under inert atmosphere to avoid thiol oxidation reactions induced by impurities.

THz Spectroscopy: The photoconductivity ($\Delta\sigma_{ph}$) measurements were performed by using an optical-pump THz-probe setup, which was driven by a Ti:sapphire laser amplifier system providing ≈50 fs laser pulses with a central wavelength of 800 nm. A pair of ZnTe nonlinear crystals were used for the generation and detection of THz electric field, which provided frequency information ranging from 0.4 to 2.5 THz. For optical-pump excitations, frequency-doubled wavelength (400 nm) generated from the fundamental wavelength (800 nm), by using a BiB_3O_6 crystal, was employed. The samples were placed under vacuum conditions (≈10^{-4} mbar) during measurements.

For the thin-film geometry, the Fourier transformation was used to convert the relative change of the THz electric field from time to frequency domain and further quantify the complex $\Delta\sigma_{ph}$ spectra based on the thin-film approximation[19]

$$\Delta\sigma_{ph}(\omega) = -\frac{n_1 + n_2}{Z_0 t_{ex}} \frac{\Delta E(\omega)}{E(\omega)} \tag{6}$$

© 2023 The Authors. Advanced Materials published by Wiley-VCH GmbH

15214095, 2023, 15, Downloaded from https://onlinelibrary.wiley.com/doi/10.1002/adma.202211157 by Cochrane France, Wiley Online Library on [13/04/2023]. See the Terms and Conditions (https://onlinelibrary.wiley.com/terms-and-conditions) on Wiley Online Library for rules of use; OA articles are governed by the applicable Creative Commons License

where $Z_0 = 377\ \Omega$ is the impedance of free space, t_{ex} is the excitation thickness, n_1 and n_2 are the refractive indices of the media before and after the sample, respectively.

To analyze the frequency-domain conductivity spectra, the Drude–Smith (DS) model was applied. The DS model described the transport of free charges experiencing backscattering processes due to, for instance, defects and/or structural deformations. The DS equation read

$$\sigma_{ph}(\omega) = \frac{\varepsilon_0 \omega_p^2 \tau}{1 - i\omega\tau}\left(1 + \frac{c}{1 - i\omega\tau}\right), \text{ with } \omega_p^2 = \frac{e^2 N}{\varepsilon_0 m^*} \quad (7)$$

where c represents the backscattering probability for carrier transport, whose value ranged from 0 (free charge) to –1 (preferential backscattering). τ, ω_p, ε_0, e, and m^* are the effective carrier momentum scattering time, plasma frequency, vacuum permittivity, elementary charge, and carrier effective mass, respectively.

To analyze the scattering times, the overall carrier scattering rate ($k_{overall}$, the inverse of scattering time) was considered taking into account the contributions from the carrier–phonon scattering (k_{phonon}) and the carrier–defect scattering (k_{defect}), following the Matthiessen's law[47]

$$k_{overall} = k_{defect} \times T^{-3/2} + k_{phonon} \times T^{\alpha} \quad (8)$$

where α is the power index. During the fitting process, identical k_{phonon} was assumed for both MoS_2 films and MoS_2–BDT networks. The fit gave: $\alpha = 0.19$ and $k_{phonon} = 4.9$ THz for both MoS_2 films and MoS_2–BDT networks, and $k_{defect} = 6.96$ THz for MoS_2 films and $k_{defect} = 4.03$ THz for MoS_2–BDT networks.

Charge-Transport Analysis: The electrical devices were measured in two-probe configuration in a customized Janis cryogenic probe station, connected to a semiconductor parameter analyzer (Keithley 4200A SCS). The chamber pressure was kept at ≈10^{-7} mbar. A Sumitomo RDK-408D2 cryogen-free closed cycle was thermally anchored to the copper sample holder and the temperature measurements were performed within the T range 340–5K. To enable statistical analysis, 48 identical devices were produced and subjected to electrical characterization.

Charge-Transport Analysis—Calculation of Localization and Average Hopping Length: For ES-VRH, the localization length ξ_{ES} was related to the characteristic temperature T_0 according to the following equation[48]

$$\xi_{ES} = \frac{2.8e^2}{\pi k_B \varepsilon \varepsilon_0 T_0} \quad (9)$$

from which the average hopping distance $R_{ES\text{-}VRH}$ was calculated as

$$R_{ES-VRH} = 0.25\left(\frac{T_0}{T}\right)^{1/2} \xi_{ES} \quad (10)$$

For 3D Mott VRH, the localization length $\xi_{3D\text{-}VRH}$ was related to the characteristic temperature T_0 as[16,18,49]

$$\xi_{3D-VRH} = \frac{24}{\pi k_B \varepsilon_0 \varepsilon_r T_0 N(E_F)} \quad (11)$$

from which the average hopping distance $R_{3D\text{-}VRH}$ was calculated as

$$R_{3D-VRH} = \frac{3}{8}\left(\frac{T_0}{T}\right)^{1/4} \xi_{3D-VRH} F_0 \quad (12)$$

where F_0 is a correction factor (equal to 1 when $T << T_0$).

In the case of the NNH, the average hopping distance R_{NNH} was related to the activation energy by the following equation

$$R_{NNH} = \left[N(E_F)E_a\right]^{1/3} \quad (13)$$

The DOS at the Fermi level [$N(E_F)$] was extrapolated from DFT calculations for the MoS_2–BDT and MoS_2–PDT networks.

The T_0 related to each hopping mechanism was extrapolated from the linear fit of the ln(σ) versus $T^{-\alpha}$ curve, as reported in Section S3 (Supporting Information). Considering the T_0 for the three systems, the hopping models were always valid within the whole T range, being $T << T_0$. The obtained values of ξ and R_{hop} were in good agreement with previous results reported in literature.[15,17]

DFT Calculations: DFT calculations were performed using the projector-augmented wave basis set using the Vienna Ab initio Simulation Package (VASP) code,[50,51] with the exchange and correlation effects treated at the Perdew–Burke–Ernzerhof (PBE) level.[52,53] Dispersion forces by Grimme correction (PBE + D2)[52,53] and dipole moment correction along the c-axis (direction perpendicular to the MoS_2 surface) were incorporated with a kinetic energy cutoff of 600 eV. Calculations were performed on MoS_2 crystals in their bulk form, replicated 4 × 4 times, using a Monkhorst–Pack sampling of $4 \times 4 \times 4$ for the Brillouin zone integration for all geometry optimizations. The geometries of MoS_2 crystals in their pristine, defective (with sulfur vacancies), and BDT/PDT network forms were fully optimized, after which self-consistent field (SCF) calculations were performed at the generalized gradient approximation (GGA)/PBE and HSE06 levels of theory using a dense K-point grid of $6 \times 6 \times 6$ and $3 \times 3 \times 3$, respectively. CDD plots were computed using $CDD = CD_{MoS_2+Mol} - CD_{MoS_2} - CD_{Mol}$, where CD_{MoS_2+Mol} is the charge density of BDT/PDT (Mol) covalent networks, CD_{MoS_2} and CD_{Mol} are the charge densities of the isolated defective MoS_2 surface and BDT/PDT molecules, respectively.

Electrical Characterization: The performance of electrical devices based on MoS_2 films and networks was evaluated by their transfer characteristics (I_{ds} vs V_{gs} curves), using a coplanar Au-gate electrode covered with 75 µL of EMI–TFSI as ionic liquid. The source–drain current (I_{ds}) was recorded sweeping the gate voltage (V_{gs}) from –2.5 to +2.5 V, at a source–drain bias V_{ds} = –0.1 V. All electrical measurements were carried out in dark and under inert atmosphere (N_2) using a Keithley 2636 A Source Meter unit. To enable statistical analysis, 24 identical devices were produced and subjected to electrical characterization. The TLM analysis was performed with the same experimental setup on devices fabricated with prepatterned substrates of channel lengths ranging from 2.5 to 20 µm. The R versus L curves of MoS_2 films and networks were fitted using allometric and linear equations, respectively.

To enable statistical analysis, 60 identical devices were produced and characterized.

Percolation Theory: Starting from the expression

$$\sigma_k(L, c_M) = A_k(c_M)\left\{\left[p_k(c_M) - p_c\right]^t + bL^{-\beta}\right\} \quad (14)$$

the ratio between measurements in two samples k, k′ at different concentrations c_M and c_M' read

$$r_{k,k'}(L, c_M, c_M') = a_{k,k'}(c_M, c_M')\frac{\left[p_k(c_M) - p_c\right]^t + bL^{-\beta}}{\left[p_{k'}(c_M') - p_c\right]^t + bL^{-\beta}} \quad (15)$$

where $a_{k,k'}(c_M, c_M') := A_k(c_M)/A_{k'}(c_M')$. As a function of L, this quantity was a sigmoid-like monotonic function, starting from a plateau value $a_{k,k'}(c_M, c'_M)$ at small L and then reaching a constant value $a_{k,k'}[p_k(c_M) - p_c]^t/[p_{k'}(c'_M) - p_c]^t$ for large L. Considering the ratios between different MoS_2 films

$$r_{k,k'}(L, 0, 0) = a_{k,k'}(0, 0)\frac{\left[p_k(0) - p_c\right]^t + bL^{-\beta}}{\left[p_{k'}(0) - p_c\right]^t + bL^{-\beta}} \quad (16)$$

no monotonic dependence on L within errors was observed, meaning that $p_k(0) \simeq p_{k'}(0)$. Hence, although different MoS_2 films had different electrical conductivities (related to the deposition steps), these variations must be considered as an effect of the different values for the average bond conductivity $A_k(0)$. The σ ratio of the MoS_2 sample before and after the BDT functionalization was defined as

$$r_{k,k}(L, c_M, 0) \simeq a_{k,k}(c_M, 0)\frac{\left[p_k(c_M) - p_c\right]^t + bL^{-\beta}}{\left[p_k(0) - p_c\right]^t + bL^{-\beta}} \quad (17)$$

All the quantities in the equation must be dimensionless, therefore $b = \mu m^{\beta}$ to be consistent with L expressed in µm. Fitting the experimental data, similar b values were observed for all samples, so it was set $b = 5.40\ \mu m^{\beta}$ calculated as their mean value.

© 2023 The Authors. Advanced Materials published by Wiley-VCH GmbH

Furthermore, the term $(p_k(0) - p_c)^t$, for every k, was negligible compared to $bL^{-\beta}$ for the L taken into account. Thus, the approximate expression

$$r_{k,k}(L,c_M,0) \simeq a_{k,k}(c_M,0)\frac{\left[p_k(c_M)-p_c\right]^t + bL^{-\beta}}{bL^{-\beta}} \tag{18}$$

with $b = 5.40\ \mu m^{\beta}$, could be used to describe the experimental data. It was worth mentioning that such a value of b indicated that finite-size effects were significant in the L range under analysis. The importance of finite-size effects was also evident from the lack of saturation in $r_{k,k}(c_M,0)$ versus L curves, expected from the exact expression.

Supporting Information

Supporting Information is available from the Wiley Online Library or from the author.

Acknowledgements

The authors acknowledge funding from the European Commission through the ERC projects SUPRA2DMAT (Grant No. GA-833707) and FUTURE-PRINT (Grant No. GA-694101), the Graphene Flagship Core 3 project (Grant No. GA-881603), and the Marie Sklodowska-Curie project ULTIMATE (Grant No. GA-813036) as well as the Agence Nationale de la Recherche through the Interdisciplinary Thematic Institute SysChem via the IdEx Unistra (Grant No. ANR-10-IDEX-0002) within the program Investissement d'Avenir, the International Center for Frontier Research in Chemistry (icFRC) and the Institut Universitaire de France (IUF). O.M. acknowledges the Alexander von Humboldt-Stiftung in the framework of the Sofja Kovalevskaja Award, endowed by the BMBF, for providing funding for this work. J.N.C. thanks the Science Foundation Ireland (SFI) for support. D.B. thanks the Energy Transition Fund of the Belgian Federal Government (FPS Economy) within the T-REX project, the Belgian National Fund for Scientific Research (FRS-FNRS) within the Consortium des Équipements de Calcul Intensif (CÉCI), under Grant No. 2.5020.11, and by the Walloon Region (ZENOBE Tier-1 supercomputer), under Grant No. 1117545. The authors thank Dr. Andrea Liscio for enlightening discussions.

Conflict of Interest

The authors declare no conflict of interest.

Author Contributions

S.I., F.U., and P.S. conceived the experiments and designed the study. S.I. and F.U. performed the electrical characterizations and charge-transport analysis. W.Z., M.B., and H.I.W. carried out the THz spectral analysis. O.M. and F.C. developed the percolation theory related to the electrical devices. C.V. performed the deposition of MoS_2 ink via spray coating. A.G.K. and J.N.C. produced and characterized the solution-processed MoS_2 ink. S.M.G. and D.B. performed and analyzed the DFT calculations. All authors discussed the results and contributed to data interpretation. S.I., F.U., and P.S. cowrote the paper with input from all coauthors.

Data Availability Statement

The data that support the findings of this study are available from the corresponding author upon reasonable request.

Keywords

charge-transport properties, covalent networks, defect engineering, electrical devices, hopping mechanisms, transition metal dichalcogenides

Received: November 29, 2022
Revised: January 7, 2023
Published online: March 3, 2023

[1] Q. H. Wang, K. Kalantar-Zadeh, A. Kis, J. N. Coleman, M. S. Strano, *Nat. Nanotechnol.* **2012**, *7*, 699.
[2] M. C. Lemme, D. Akinwande, C. Huyghebaert, C. Stampfer, *Nat. Commun.* **2022**, *13*, 1392.
[3] F. Bonaccorso, A. Lombardo, T. Hasan, Z. Sun, L. Colombo, A. C. Ferrari, *Mater. Today* **2012**, *15*, 564.
[4] Y. Hernandez, V. Nicolosi, M. Lotya, F. M. Blighe, Z. Sun, S. De, I. T. McGovern, B. Holland, M. Byrne, Y. K. Gun'Ko, J. J. Boland, P. Niraj, G. Duesberg, S. Krishnamurthy, R. Goodhue, J. Hutchison, V. Scardaci, A. C. Ferrari, J. N. Coleman, *Nat. Nanotechnol.* **2008**, *3*, 563.
[5] S. Pinilla, J. Coelho, K. Li, J. Liu, V. Nicolosi, *Nat. Rev. Mater.* **2022**, *7*, 717.
[6] S. Bertolazzi, M. Gobbi, Y. Zhao, C. Backes, P. Samorì, *Chem. Soc. Rev.* **2018**, *47*, 6845.
[7] Z. Hu, Z. Wu, C. Han, J. He, Z. Ni, W. Chen, *Chem. Soc. Rev.* **2018**, *47*, 3100.
[8] D. Qi, C. Han, X. Rong, X.-W. Zhang, M. Chhowalla, A. T. S. Wee, W. Zhang, *ACS Nano* **2019**, *13*, 9464.
[9] S. Ippolito, A. Ciesielski, P. Samorì, *Chem. Commun.* **2019**, *55*, 8900.
[10] Y. Wang, Y. Zheng, C. Han, W. Chen, *Nano Res.* **2021**, *14*, 1682.
[11] S. Ippolito, P. Samorì, *Small Sci.* **2022**, *2*, 2100122.
[12] V. Nicolosi, M. Chhowalla, M. G. Kanatzidis, M. S. Strano, J. N. Coleman, *Science* **2013**, *340*, 1226419.
[13] A. G. Kelly, D. O'Suilleabhain, C. Gabbett, J. N. Coleman, *Nat. Rev. Mater.* **2022**, *7*, 217.
[14] S. Ippolito, A. G. Kelly, R. Furlan de Oliveira, M.-A. Stoeckel, D. Iglesias, A. Roy, C. Downing, Z. Bian, L. Lombardi, Y. A. Samad, V. Nicolosi, A. C. Ferrari, J. N. Coleman, P. Samorì, *Nat. Nanotechnol.* **2021**, *16*, 592.
[15] H. Qiu, T. Xu, Z. Wang, W. Ren, H. Nan, Z. Ni, Q. Chen, S. Yuan, F. Miao, F. Song, G. Long, Y. Shi, L. Sun, J. Wang, X. Wang, *Nat. Commun.* **2013**, *4*, 2642.
[16] J. Xue, S. Huang, J.-Y. Wang, H. Q. Xu, *RSC Adv.* **2019**, *9*, 17885.
[17] J. S. Kim, J. Kim, J. Zhao, S. Kim, J. H. Lee, Y. Jin, H. Choi, B. H. Moon, J. J. Bae, Y. H. Lee, S. C. Lim, *ACS Nano* **2016**, *10*, 7500.
[18] E. Piatti, A. Arbab, F. Galanti, T. Carey, L. Anzi, D. Spurling, A. Roy, A. Zhussupbekova, K. A. Patel, J. M. Kim, D. Daghero, R. Sordan, V. Nicolosi, R. S. Gonnelli, F. Torrisi, *Nat. Electron.* **2021**, *4*, 893.
[19] R. Ulbricht, E. Hendry, J. Shan, T. F. Heinz, M. Bonn, *Rev. Mod. Phys.* **2011**, *83*, 543.
[20] W. Zheng, B. Sun, D. Li, S. M. Gali, H. Zhang, S. Fu, L. Di Virgilio, Z. Li, S. Yang, S. Zhou, D. Beljonne, M. Yu, X. Feng, H. I. Wang, M. Bonn, *Nat. Phys.* **2022**, *18*, 544.
[21] W. Zheng, N. F. Zorn, M. Bonn, J. Zaumseil, H. I. Wang, *ACS Nano* **2022**, *16*, 9401.
[22] W. Zheng, M. Bonn, H. I. Wang, *Nano Lett.* **2020**, *20*, 5807.
[23] H. Shi, S. Fu, Y. Liu, C. Neumann, M. Wang, H. Dong, P. Kot, M. Bonn, H. I. Wang, A. Turchanin, O. G. Schmidt, A. Shaygan Nia, S. Yang, X. Feng, *Adv. Mater.* **2021**, *33*, 2105694.
[24] N. F. Mott, *Metal–Insulator Transitions*, Taylor & Francis, London, UK **1990**.

© 2023 The Authors. Advanced Materials published by Wiley-VCH GmbH

15214095, 2023, 15, Downloaded from https://onlinelibrary.wiley.com/doi/10.1002/adma.202211157 by Cochrane France, Wiley Online Library on [13/04/2023]. See the Terms and Conditions (https://onlinelibrary.wiley.com/terms-and-conditions) on Wiley Online Library for rules of use; OA articles are governed by the applicable Creative Commons License

[25] N. F. Mott, E. A. Davis, *Electronic Processes in Non-Crystalline Materials*, Clarendon Press, Oxford, UK **2012**.
[26] I. S. Beloborodov, A. V. Lopatin, V. M. Vinokur, K. B. Efetov, *Rev. Mod. Phys.* **2007**, *79*, 469.
[27] T. Carey, A. Arbab, L. Anzi, H. Bristow, F. Hui, S. Bohm, G. Wyatt-Moon, A. Flewitt, A. Wadsworth, N. Gasparini, J. M. Kim, M. Lanza, I. McCulloch, R. Sordan, F. Torrisi, *Adv. Electron. Mater.* **2021**, *7*, 2100112.
[28] F.-C. Chiu, *Adv. Mater. Sci. Eng.* **2014**, *2014*, 578168.
[29] T. B. Schrøder, J. C. Dyre, *Phys. Rev. Lett.* **2000**, *84*, 310.
[30] D. Yu, C. Wang, B. L. Wehrenberg, P. Guyot-Sionnest, *Phys. Rev. Lett.* **2004**, *92*, 216802.
[31] R. Debbarma, N. H. L. Nguyen, V. Berry, *Appl. Mater. Today* **2021**, *23*, 101072.
[32] B. I. Shklovskii, A. L. Efros, *Electronic Properties of Doped Semiconductors*, Springer, Berlin, Germany **1984**.
[33] A. L. Efros, B. I. Shklovskii, *J. Phys. C: Solid State Phys.* **1975**, *8*, L49.
[34] J.-H. Chen, C. Jang, S. Xiao, M. Ishigami, M. S. Fuhrer, *Nat. Nanotechnol.* **2008**, *3*, 206.
[35] C.-L. Wu, H. Yuan, Y. Li, Y. Gong, H. Y. Hwang, Y. Cui, *Nano Lett.* **2018**, *18*, 2387.
[36] J. He, K. Hummer, C. Franchini, *Phys. Rev. B* **2014**, *89*, 075409.
[37] J. Hong, Z. Hu, M. Probert, K. Li, D. Lv, X. Yang, L. Gu, N. Mao, Q. Feng, L. Xie, J. Zhang, D. Wu, Z. Zhang, C. Jin, W. Ji, X. Zhang, J. Yuan, Z. Zhang, *Nat. Commun.* **2015**, *6*, 6293.
[38] Y. Sun, X. Wang, X.-G. Zhao, Z. Shi, L. Zhang, *J. Semicond.* **2018**, *39*, 072001.
[39] S. Bertolazzi, S. Bonacchi, G. Nan, A. Pershin, D. Beljonne, P. Samorì, *Adv. Mater.* **2017**, *29*, 1606760.
[40] S. M. Gali, A. Pershin, A. Lherbier, J.-C. Charlier, D. Beljonne, *J. Phys. Chem. C* **2020**, *124*, 15076.
[41] J. Li, M. M. Naiini, S. Vaziri, M. C. Lemme, M. Östling, *Adv. Funct. Mater.* **2014**, *24*, 6524.
[42] S. H. Kim, K. Hong, W. Xie, K. H. Lee, S. Zhang, T. P. Lodge, C. D. Frisbie, *Adv. Mater.* **2013**, *25*, 1822.
[43] A. G. Kelly, T. Hallam, C. Backes, A. Harvey, A. S. Esmaeily, I. Godwin, J. Coelho, V. Nicolosi, J. Lauth, A. Kulkarni, S. Kinge, L. D. A. Siebbeles, G. S. Duesberg, J. N. Coleman, *Science* **2017**, *356*, 69.
[44] B. Derrida, J. Vannimenus, *J. Phys. A: Math. Gen.* **1982**, *15*, L557.
[45] M. van Hecke, *J. Phys.: Condens. Matter* **2010**, *22*, 033101.
[46] C. Backes, R. J. Smith, N. McEvoy, N. C. Berner, D. McCloskey, H. C. Nerl, A. O'Neill, P. J. King, T. Higgins, D. Hanlon, N. Scheuschner, J. Maultzsch, L. Houben, G. S. Duesberg, J. F. Donegan, V. Nicolosi, J. N. Coleman, *Nat. Commun.* **2014**, *5*, 4576.
[47] C. Jacoboni, *Theory of Electron Transport in Semiconductors: A Pathway from Elementary Physics to Nonequilibrium Green Functions*, Springer, New York **2010**.
[48] R. Rosenbaum, R. Haberkern, P. Häussler, E. Palm, T. Murphy, S. Hannahs, B. Brandt, *J. Phys.: Condens. Matter* **2000**, *12*, 9735.
[49] M. J. M. Jimenez, R. F. Oliveira, T. P. Almeida, R. C. H. Ferreira, C. C. B. Bufon, V. Rodrigues, M. A. Pereira-da-Silva, Â. L. Gobbi, M. H. O. Piazzetta, A. Riul, *Nanotechnology* **2017**, *28*, 495711.
[50] G. Kresse, J. Furthmüller, *Phys. Rev. B* **1996**, *54*, 11169.
[51] G. Kresse, D. Joubert, *Phys. Rev. B* **1999**, *59*, 1758.
[52] J. P. Perdew, K. Burke, M. Ernzerhof, *Phys. Rev. Lett.* **1996**, *77*, 3865.
[53] S. Grimme, *J. Comput. Chem.* **2006**, *27*, 1787.

© 2023 The Authors. Advanced Materials published by Wiley-VCH GmbH

15214095, 2023, 15, Downloaded from https://onlinelibrary.wiley.com/doi/10.1002/adma.202211157 by Cochrane France, Wiley Online Library on [13/04/2023]. See the Terms and Conditions (https://onlinelibrary.wiley.com/terms-and-conditions) on Wiley Online Library for rules of use; OA articles are governed by the applicable Creative Commons License

ADVANCED MATERIALS

Supporting Information

for *Adv. Mater.,* DOI: 10.1002/adma.202211157

Unveiling Charge-Transport Mechanisms in Electronic Devices Based on Defect-Engineered MoS_2 Covalent Networks

*Stefano Ippolito, Francesca Urban, Wenhao Zheng, Onofrio Mazzarisi, Cataldo Valentini, Adam G. Kelly, Sai Manoj Gali, Mischa Bonn, David Beljonne, Federico Corberi, Jonathan N. Coleman, Hai I. Wang, and Paolo Samorì**

Supporting Information

Unveiling charge-transport mechanisms in electronic devices based on defect-engineered MoS_2 covalent networks

*Stefano Ippolito, Francesca Urban, Wenhao Zheng, Onofrio Mazzarisi, Cataldo Valentini, Adam G. Kelly, Sai Manoj Gali, Mischa Bonn, David Beljonne, Federico Corberi, Jonathan N. Coleman, Hai I. Wang, Paolo Samorì**

Table of Contents

1. Multiscale characterization of solution-processed MoS_2 ______ S2
2. THz spectral investigation of MoS_2 films and networks ______ S3
3. Charge transport analysis ______ S4
4. DFT calculations of MoS_2 networks: π-conjugated *vs*. aliphatic dithiolated molecules ______ S10
5. Electrical characterization of MoS_2 films and networks ______ S13
6. Percolation theory of electrical devices based on MoS_2 films and networks ______ S19
7. References ______ S22

1. Multiscale characterization of solution-processed MoS_2

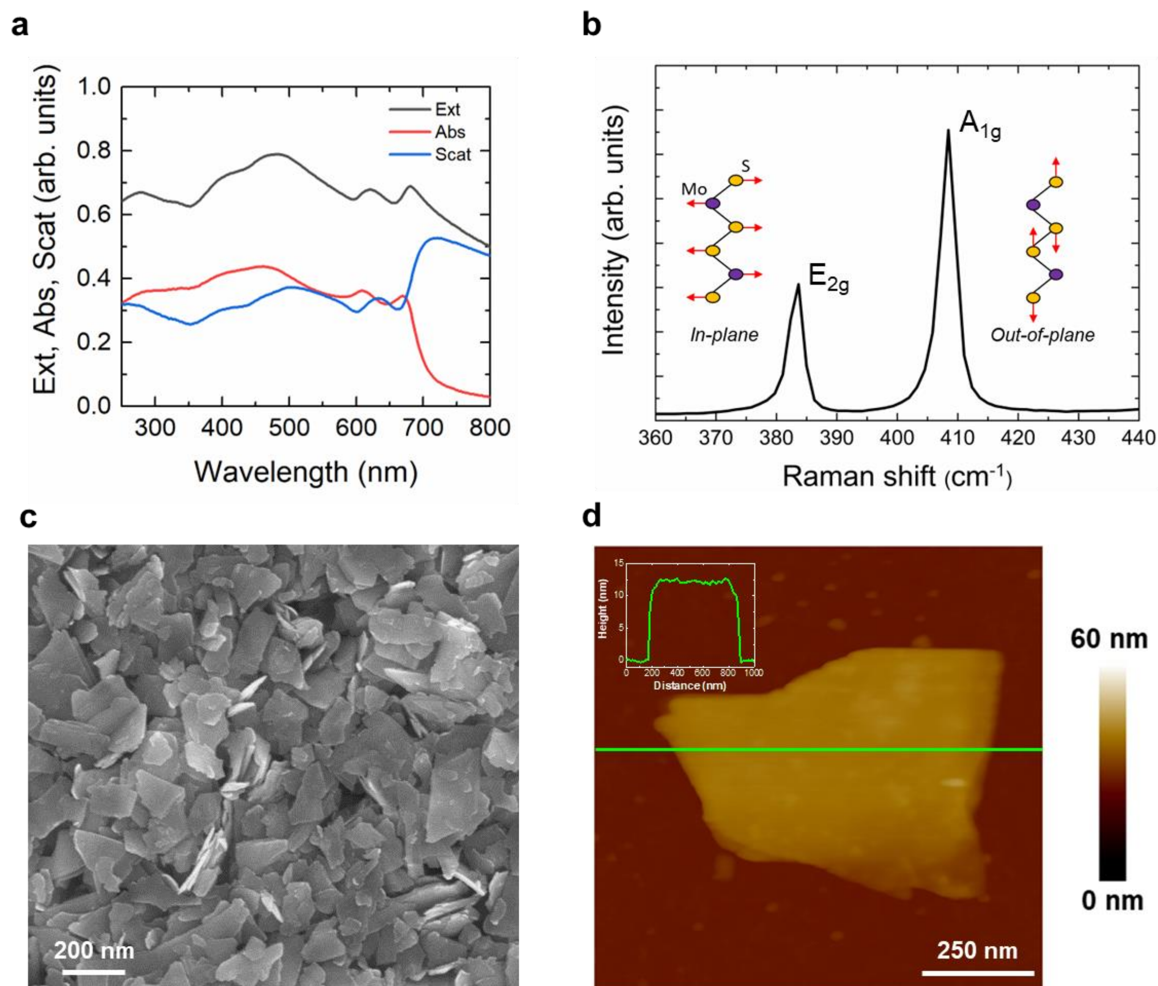

Figure S1. a) UV-Vis extinction (Ext), absorbance (Abs) and scattering (Scat) spectra for MoS_2 ink at 10 μg/ml. The scattering spectrum is obtained by subtracting the absorbance spectrum from the extinction spectrum. b) Raman spectrum of a spray-coated MoS_2 thin film. Characteristic E^1_{2g} and A_{1g} Raman modes are also highlighted, due to in-plane and out-of-plane vibrations, respectively. c) SEM image of a spray-coated MoS_2 thin film. d) Representative AFM image of a MoS_2 flake, whose height profile is shown as inset.

2. THz spectral investigation of MoS2 films and networks

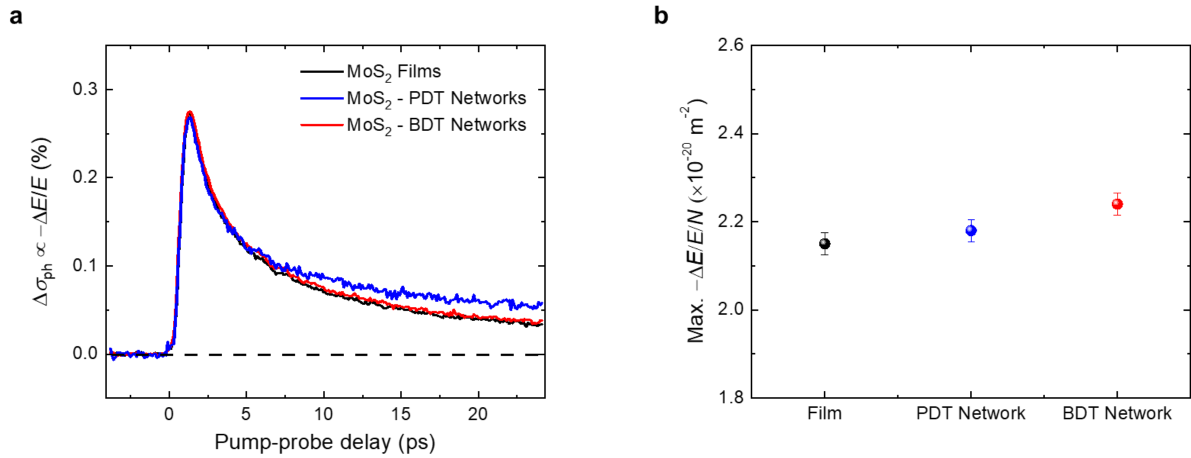

Figure S2. a) $\Delta\sigma_{ph}$ dynamics of pristine MoS_2 films, MoS_2-PDT networks and MoS_2-BDT networks. The samples are excited by 3.10 eV laser pulses. b) Maximum $\Delta\sigma_{ph}$ normalized by the incident photon density for the three samples.

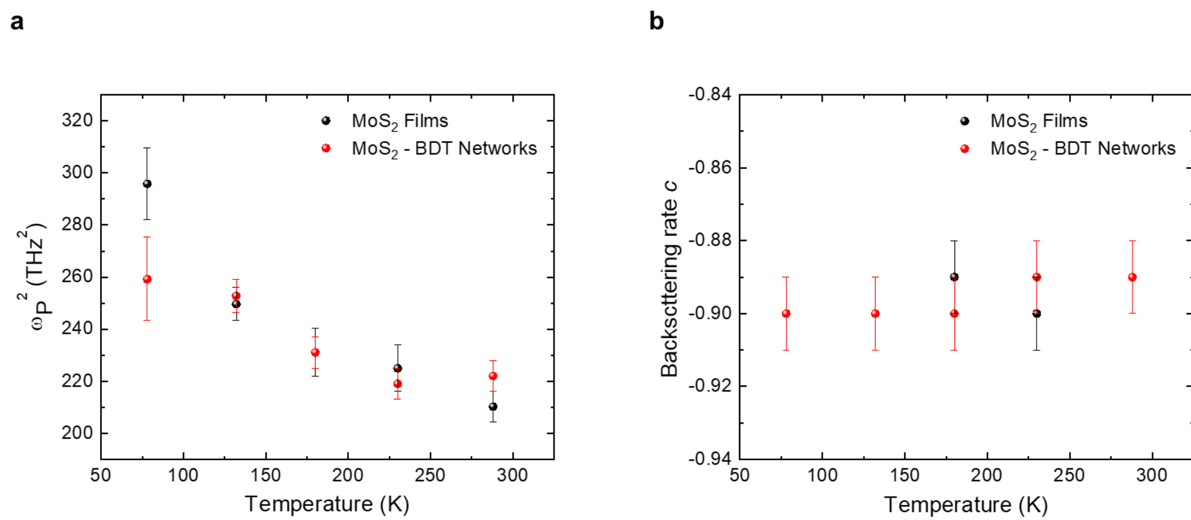

Figure S3. a) ω_P^2 (proportional to carrier density) and b) backscattering rate as a function of T for MoS_2 films and MoS_2-BDT networks.

3. Charge transport analysis

The charge carrier transport in poorly conductive systems can be ruled by several conduction mechanisms, which are distinguished in electrode-limited and bulk-limited[1,2]. For the former, the charge transport strictly depends on the interface between the electrode and the semiconducting material, whereas for the latter it is related to the intrinsic material properties. T-dependent measurements represent an efficient strategy to identify distinct conduction regimes. To this end, we perform current-voltage (I-V) measurements in the T range 340–5 K. From σ *vs*. T curves (**Figure 2**b) we observe an exponential behavior within 340-200 K, a transient regime within 200-150 K and a saturation regime between 150 and 5 K pointing to a T-independent behavior. The I-V curves in the range 340-200 K are displayed in **Figure S4**.

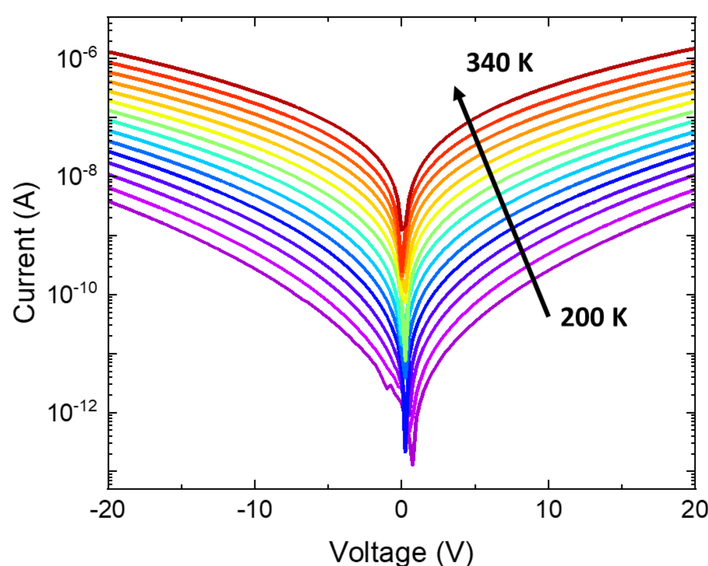

Figure S4. I-V characteristic curves for pristine MoS_2 films within the T-range 340-200 K.

In disordered and defective systems, hopping is one of the most common conduction mechanisms with an exponential dependence of σ on T, involving localized defective states[2–5]. At finite T, the charge carriers, strongly localized within a correlation length ξ, move through localized defect/trap states via two possible mechanisms:

(i) Variable Range Hopping (VRH)
- Mott VRH
- Efros-Shklovskii VRH

ii) Nearest Neighbor Hopping (NNH)

Writing the resistivity of the system as

$$\rho = \rho_0 exp\left(\frac{T_0}{T}\right)^{\alpha} \quad (S1)$$

the hopping mechanisms can be distinguished by the exponent α. To extrapolate α, we define the function W[6,7] as

$$W = -\frac{T}{\rho}\frac{d\rho}{dT} \quad (S2)$$

By substituting **Equation S1** into **Equation S2** and linearizing the resulting expression, we obtain

$$ln\, W = -\alpha\, ln\, T + constant \quad (S3)$$

The slope of the linear fit returns α, which denotes the hopping conduction mechanism[8–11]. The hopping between localized states is characterized by an average hopping distance R_{hop}, as a result of the balance: (i) between the shortest possible hopping distance and the smallest energy difference of the available localized states, for VRH regime; (ii) the direct hop between the spatially closest localized states, regardless their energy difference, for NNH regime[3,4,12]. As presented in the Main Text, our MoS_2 films and networks present three different conduction mechanisms depending on the functionalizing molecule. The hopping transport mechanism and the parameters of the model, extrapolated from the equation described in the Methods section, are reported in **Table S1**.

	Hopping mechanism	$\boldsymbol{T_0}$ **(K)**	$\boldsymbol{\xi}$ **(nm)**	$\boldsymbol{R_{hop}}$ **(nm)**
MoS_2 Films	ES-VRH	2.7 ± 0.4 x 10^5	0.14 ± 0.01	1.10 ± 0.10
MoS_2-PDT Networks	3D-Mott VRH	2.3 ± 0.6 x 10^9	0.13 ± 0.01	2.50 ± 0.10
MoS_2-BDT Networks	NNH	n.a.	n.a.	1.20 ± 0.01

Table S1. Hopping mechanism, characteristic temperature (T_0), correlation length (ξ) and average hopping distance (R_{hop}) for the MoS_2 films and networks.

The characteristic temperature (T_0) is calculated for MoS_2 films and MoS_2-PDT networks from the slope of the $ln\,(\sigma)\ vs.\ T^{-\alpha}$ plot (**Figure S5**).

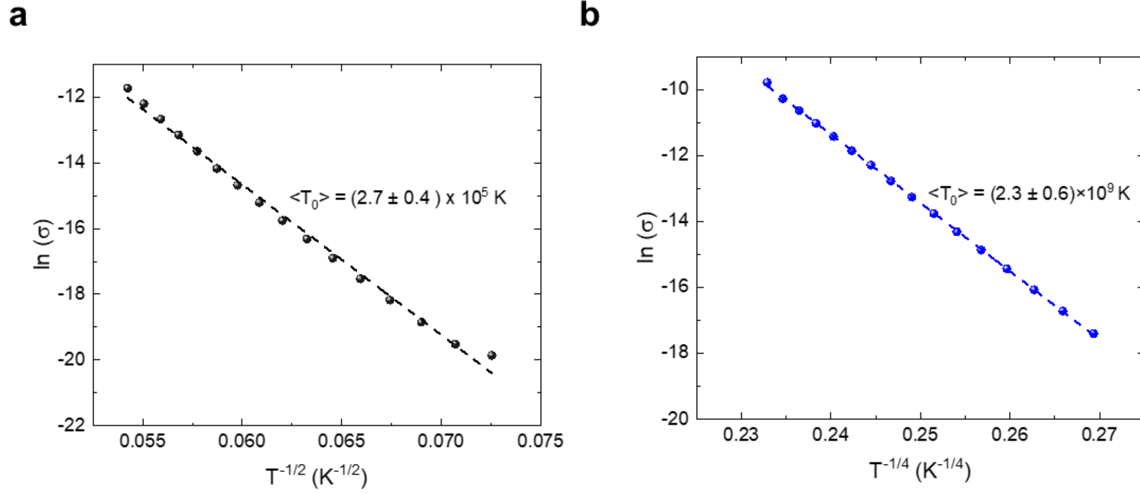

Figure S5. $ln\ (\sigma)\ vs.\ T^{-\alpha}$ plots for a) MoS_2 films and b) MoS_2-PDT networks. The reported value is the mean and standard deviation of 6 devices.

For the MoS_2-BDT networks the hopping distance is calculated considering the following relation

$$R_{NNH} = [N(E_F)E_a]^{1/3} \tag{S4}$$

where E_a is the activation energy of the system ($< E_a >$ = 285 ± 5 meV) extrapolated from the linear fit of the curves shown in **Figure S6**.

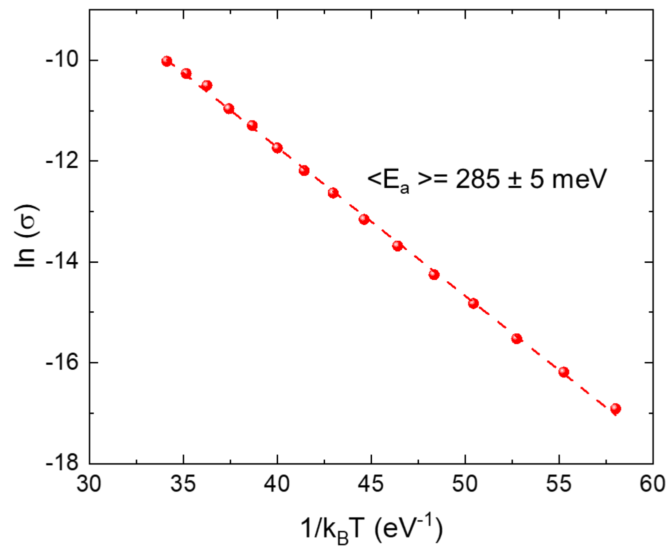

Figure S6. Arrhenius plot for the calculation of E_a in MoS_2-BDT networks. The reported value is the mean and standard deviation of 6 devices.

To distinguish among different hopping mechanisms, we extract the parameter α from $ln(W)$ $vs.$ $ln(T)$ plots. In this regard, such an analysis is performed at V = 1 V for all systems.

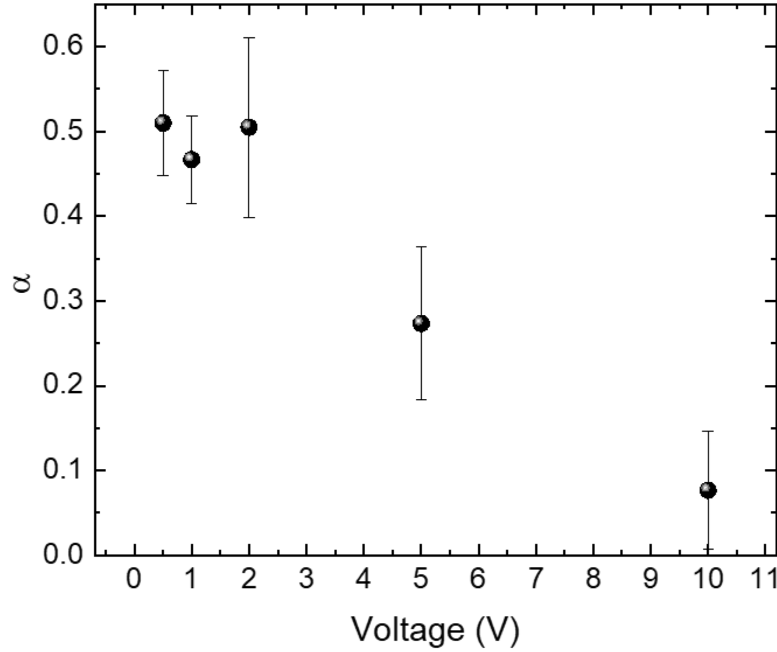

Figure S7. Extracted α values at different bias voltages for MoS_2 films.

Figure S7 displays α values as a function of different bias voltages. At high V, α shows a strong dependence on the voltage, likely due to influence of the effective temperature[13]. At low V (< 2 V), α results constant. Thus, we consider α extracted at 1 V for our analysis, being in the V-independent region of α $vs.$ V plot and sufficiently high to provide a measurable current in the whole T range.

For T <150 K, the σ $vs.$ T plots for all systems display a T-independent behavior, pointing to a different transport mechanism. Due to the minimal thermal energy, the charge carriers can tunnel through a barrier only when a sufficient high potential is applied between the electrodes (**Figure S8**a). The tunneling probability depends on the shape of the barrier (defined by the applied voltage) and leads to two different tunnelling mechanisms. At low bias, the barrier is rectangular and the $I-E$ relation is described by the direct tunneling[1]

$$I \propto E \exp\left(-\frac{4\pi\sqrt{2m}\phi}{h}\right) \tag{S5}$$

where I is the device current, E is the electric field, m is the electron tunneling effective mass and Φ the tunneling barrier height.

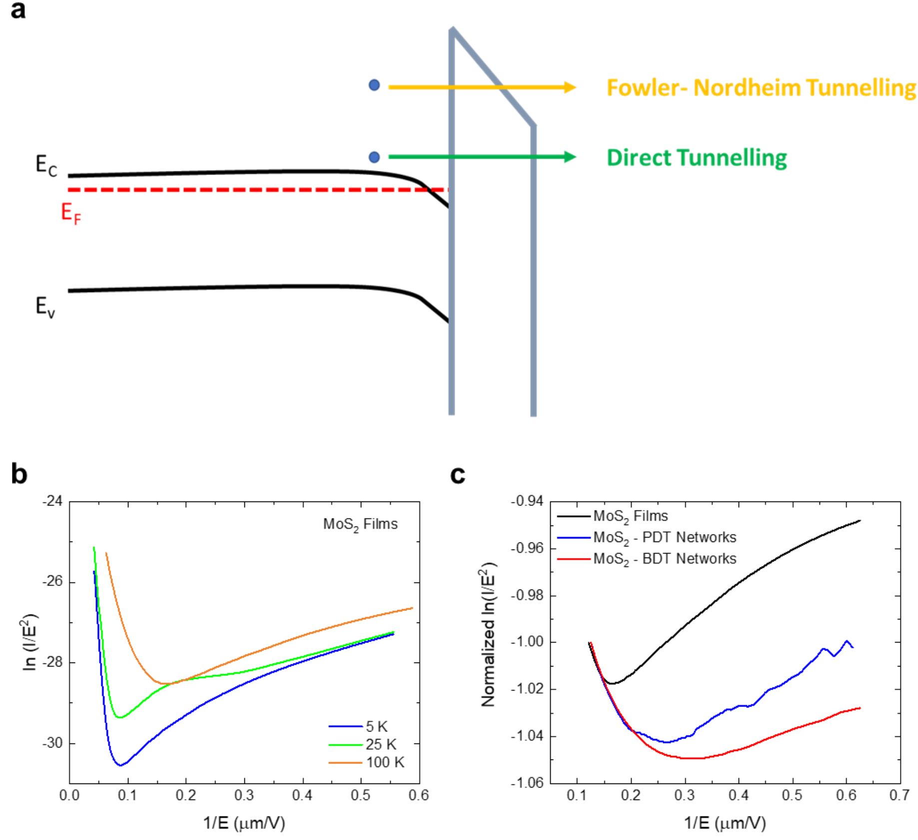

Figure S8. a) Schematic of the tunneling processes. b) Fowler-Nordheim curves at low *T* (5-100 K) for MoS_2 films. c) normalized FN curves at 100 K for MoS_2 films, MoS_2- PDT and MoS_2-BDT networks.

At bias higher than Φ, the barrier shape becomes triangular, increasing the tunneling probability. The Fowler–Nordheim (FN) tunneling (*i.e.*, field emission) describes this scenario with the following $I-E$ relationship

$$I \propto E^2 \exp\left(-\frac{8\pi\sqrt{2m^*}\phi^3}{3h\,E}\right) \quad \text{(S6)}$$

The FN tunneling plot $ln\ (I/E^2)$ *vs.* $1/E$ leads to a linear trend with negative slope, while the direct tunneling displays a linear dependence on $ln(1/E)$

$$\ln\left(\frac{I}{E^2}\right) \propto -\frac{1}{E} \quad \text{Fowler − Nordheim Tunneling} \quad \text{(S7)}$$

$$\ln\left(\frac{I}{E^2}\right) \propto \ln\left(\frac{1}{E}\right) \quad \text{Direct Tunneling} \quad \text{(S8)}$$

The two regimes can be identified in the $ln\ (I/E^2)$ *vs.* $1/E$ plot, as shown in **Figure S8**b-c for T range 100-5 K. The transition field (E_{tr}) between the two tunneling regimes is reported in **Table S2** for MoS_2 films, MoS_2-PDT networks and MoS_2-BDT networks.

	$1/E_{tr}$ $(\mu m/V)$
MoS_2 Films	0.20 ± 0.03
MoS_2-PDT Networks	0.36 ± 0.13
MoS_2-BDT Networks	0.32 ± 0.03

Table S2. Evaluation of E_{tr} between the FN and the direct tunneling regime for MoS_2 films, MoS_2-PDT networks and MoS_2-BDT networks.

4. DFT calculations of MoS_2 networks: *π*-conjugated *vs*. aliphatic dithiolated molecules

Starting from pristine MoS_2 crystals, V_S are created by removing two sulfur atoms either directly on top of each other or diagonally to each other, such that the V_S concentration is kept at 6% in both cases. These two defective MoS_2 forms are referred to as configuration 1 and configuration 2, respectively. Even though their crystal structure parameters show small variations when compared to the pristine form (**Table S3**), considerable differences are observed between their electronic structures. Although configuration 1 exhibits mid-gap defect states that are highly localized within the electronic band gap (**Figure S9**), the defects states are spread through the electronic band gap for configuration 2 (**Figure S10**). These variations can be attributed to the differences in the nature of the electronic wavefunction at the defect states caused by the interacting V_S.

	a (Å)	**b (Å)**	**c (Å)**	**α (°)**	**β (°)**	**γ (°)**	**Volume (Å^3)**
MoS_2 pristine	12.72	12.72	6.86	90	90	120	963.68
MoS_2-2V_S configuration 1	12.59	12.59	6.79	90	90	120	934.11
MoS_2-2V_S configuration 2	12.63	12.63	6.76	90	90	120	934.63

Table S3. DFT-optimized lattice parameters of AA-stacked pristine MoS_2 crystals as well as MoS_2-2V_S, both configuration 1 and configuration 2.

	Γ — K	**Γ — A**	**K — Γ**	**K — A**	**d_c (Å)**
MoS_2 Pristine	0.270	0.971	0.255	0.189	6.85
MoS_2-2V_S	0.932	0.791	0.403	0.238	6.76
MoS_2-PDT Networks	0.799	2.274	0.246	0.271	9.09
MoS_2-BDT Networks	1.251	1.091	0.226	0.188	9.69

Table S4. Electron effective masses (m^*) at the CBE obtained along the high symmetry points. Both K—Γ and K—A correspond to the primary directions, as K represents the CBE. Notably, m^* values for MoS_2-BDT networks are significantly lower than MoS_2-2V_S and MoS_2-PDT networks, highlighting an enhanced inter-flake electronic connectivity.

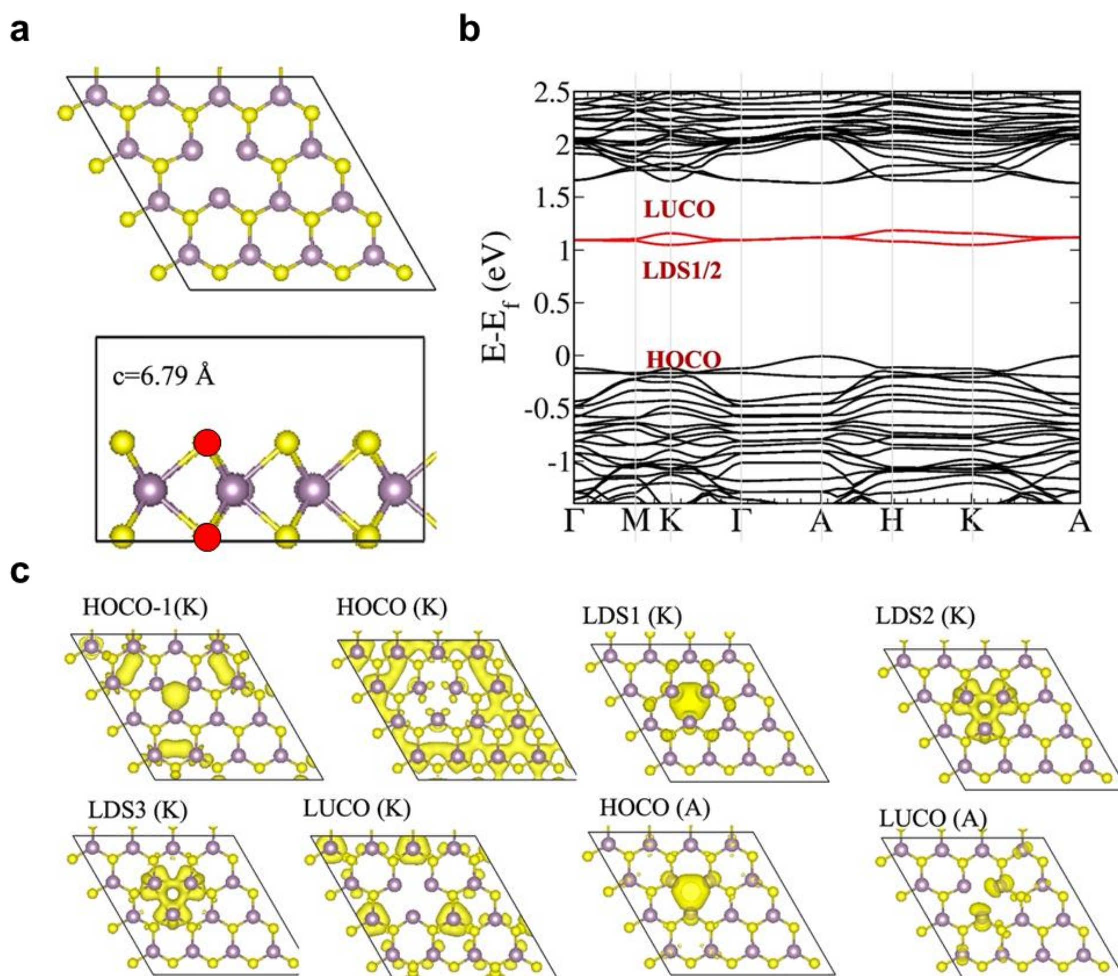

Figure S9. a) Sketch and b) electronic structure of MoS_2-$2V_S$ (6% V_S) in configuration 1, as well as c) the related crystalline orbitals. HOCO and LUCO represent the crystalline orbitals at the valence and conduction band edges (*i.e.*, VBE and CBE), respectively, whereas the LDS represent the crystalline orbitals of localized defect states (indicated by red circles). In brackets, the symmetry points where the crystalline orbitals are obtained.

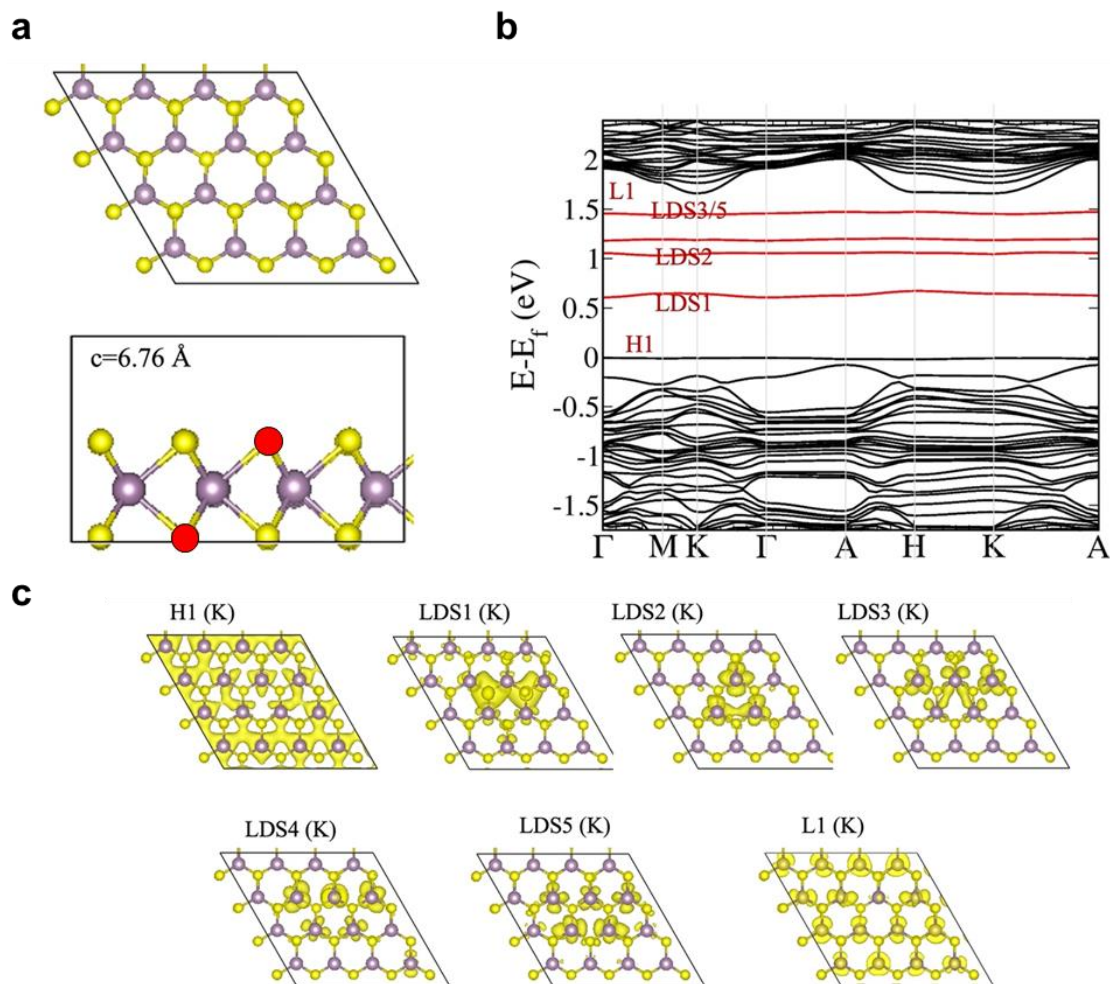

Figure S10. a) Sketch and b) electronic structure of MoS_2-2V_S (6% V_S) in configuration 2, as well as c) the related crystalline orbitals. HOCO and LUCO represent the crystalline orbitals at the valence and conduction band edges (*i.e.*, VBE and CBE), respectively, whereas the LDS represent the crystalline orbitals of localized defect states (indicated by red circles). In brackets, the symmetry points where the crystalline orbitals are obtained.

5. Electrical characterization of MoS_2 films and networks

<u>Functionalization time and BDT concentration</u>

To ensure an efficient penetration of the functionalizing molecules across the whole film, we measure the electrical properties of MoS_2 films upon different exposure times to BDT, namely 24 h, 48 h and 96 h (**Figure S11**a).

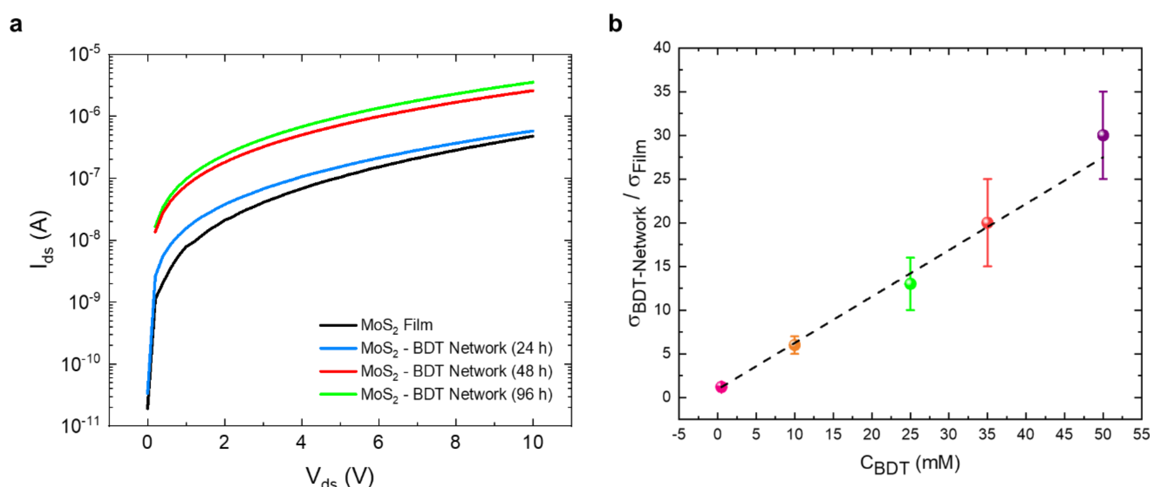

Figure S11. a) I-V curves of MoS_2 films and MoS_2-BDT networks upon BDT exposure for 24 h, 48 h and 96 h. b) $\sigma_{BDT-Network}/\sigma_{film}$ as a function of BDT concentration.

The I-V curves for MoS_2 films and MoS_2-BDT networks (24 h) do not reveal significant differences in terms of σ, indicating a negligible effect of the functionalization. However, the increase of the functionalization time to 48 h leads to a difference by one order of magnitude in the device current (red curve). A further increase in the BDT reaction time up to 96 h does not particularly improve the network conductivity. Thus, a proper tuning of the functionalization time is needed according to the deposition technique adopted for the device fabrication. This is to ascribe, as reported by Kelly et al.[14], to the morphology of solution-processed TMD films, which is governed by a complex interplay between exfoliation steps, flake size (*i.e.*, thickness and lateral size), as well as deposition method, leading to different morphological features according to the operating conditions.

We also measured the conductivity of covalent MoS_2 networks made by using 5 different BDT concentrations (keeping a constant reaction time at 48 h). The results are reported in **Figure S11**b where a linear trend is highlighted.

For the characterization of our printed devices, we choose a functionalization time of 48 h.

Electrical device performance

As shown in **Figure S11**, the exposure to BDT dithiolated molecules promotes an enhancement of electrical performance by one order of magnitude with respect to pristine MoS_2 films. This is consistent with the passivation of V_S and inter-flake bridging by BDT molecules. The field-effect mobility (μ_{FE}) in our devices is calculated from the characteristic transfer curves (I_{ds} *vs.* V_{gs}) according to the following relation

$$\mu_{FE} = \frac{g_m L}{W V_{ds} C_v t} \quad \text{(S9)}$$

where g_m is ($\partial I_{ds} / \partial V_{gs}$), L is the channel length, C_v is the volumetric capacitance, V_{ds} is the source-drain voltage, W is the channel width and t is the thickness of the MoS_2 film.

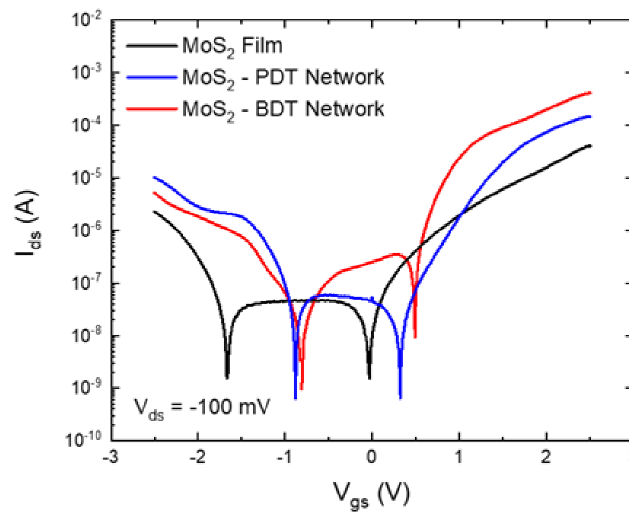

Figure S12. Transfer characteristics of MoS_2 films, MoS_2-PDT networks and MoS_2-BDT networks on logarithmic scale.

The main device figures of merit for MoS_2 films and networks are reported in the **Table S5**.

	μ_{FE} (cm^2/ V s)	I_{ON}/I_{OFF}	V_{th} (V)
MoS_2 Films	$1.4 \pm 0.6 \times 10^{-3}$	$2 \pm 1 \times 10^3$	2.06 ± 0.02
MoS_2-PDT Networks	$5.8 \pm 0.9 \times 10^{-3}$	$3 \pm 1 \times 10^3$	1.99 ± 0.05
MoS_2-BDT Networks	$1.2 \pm 0.7 \times 10^{-2}$	$2 \pm 1 \times 10^4$	1.99 ± 0.04

Table S5. Device figures-of-merit for MoS_2 films and networks. The reported value is the mean and standard deviation of 24 devices.

Extrapolation of the Schottky barrier

To evaluate the Schottky barrier at Au/MoS_2 interface, we investigate the current *vs.* electric field (I-E) characteristics before and after thiol functionalization as function of T (**Figure S13**a).

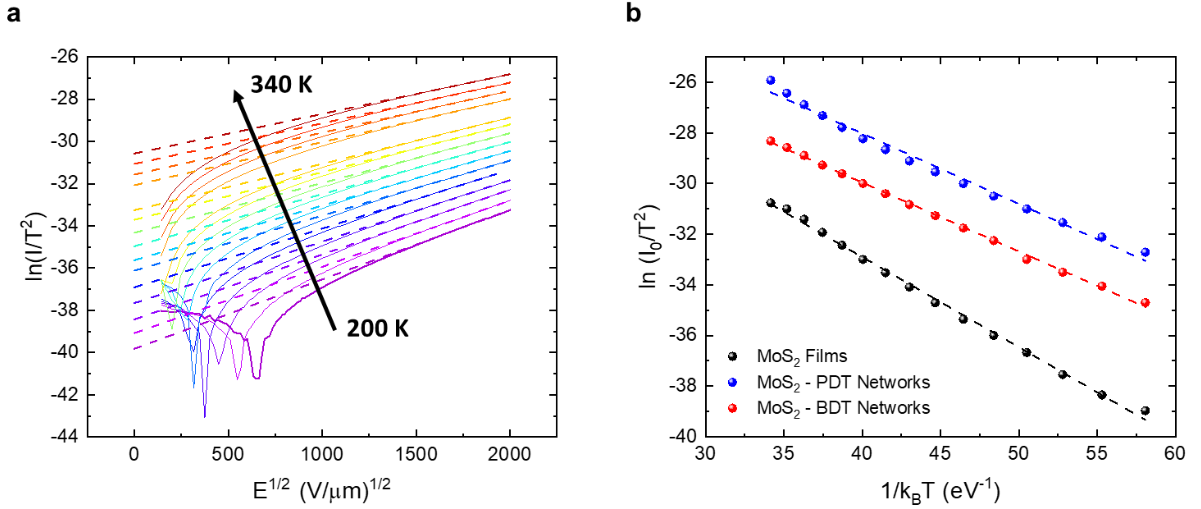

Figure S13. a) $ln\ (I/T^2)$ *vs.* $E^{1/2}$ for MoS_2 pristine films within 340-200 K and b) Arrhenius plot of Schottky emission for MoS_2 films, MoS_2-PDT networks and MoS_2-BDT networks. Φ_{SB} values are reported in Table S6.

The curves are considered within the T range 340-200 K and all systems exhibit characteristic I-E in agreement with Schottky emission, where $ln\ (I/T^2\ )$ *vs.* $E^{1/2}$ is a linear plot according to

$$I = A\,A * T^2\,exp\left[-\frac{q}{k_BT}\left(\phi_B - \sqrt{\frac{qE}{4\pi\varepsilon_r\varepsilon_0}}\right)\right] \quad \text{(S10)}$$

where A is the charge injection area, A^* is the effective Richardson constant, T is the absolute temperature, k_B is the Boltzmann constant, Φ_{SB} is the Schottky barrier height, ε_r is the MoS_2 dielectric constant (4.8 for multilayer MoS_2)[15] and ε_0 the free-space permittivity. Considering the slope of $ln\ (I_0/T^2)$ *vs.* $1/k_BT$, we get Φ_{SB} from the Arrhenius plot (**Figure S13**b).

Table S6 summarized the Φ_{SB} values for the three systems under analysis, in good agreement with previous reports[15]. The lowering of Φ_{SB} in MoS_2 networks is ascribed to the healing of interface defects (Au/MoS_2 interface) by both PDT and BDT molecules[16].

	Φ_{SB} (meV)
MoS_2 Films	355 ± 15
MoS_2-PDT Networks	270 ± 25
MoS_2-BDT Networks	270 ± 5

Table S6. Φ_{SB} calculated from the Arrhenius plot for MoS_2 films, MoS_2-PDT and MoS_2-BDT networks. The reported value is the mean and standard deviation of 24 devices.

Transmission length method

In an electrical device the total resistance R_T is given by the combination of the contact resistance R_C, channel resistance $R_{channel}$ and the metal resistance R_m. Assuming $R_m \ll R_C$ and $R_{channel}$ and thus neglecting the metal resistance, the total resistance can be written as[17,18]

$$R_T = nR_C + R_{channel}(L) \quad \text{(S11)}$$

where n indicates the number of interdigitated electrodes (22 in our device geometry) and $R_{channel}$ determines the L-dependence of R_T.

A schematic of the device and the design electrode configuration are displayed in **Figure S14**.

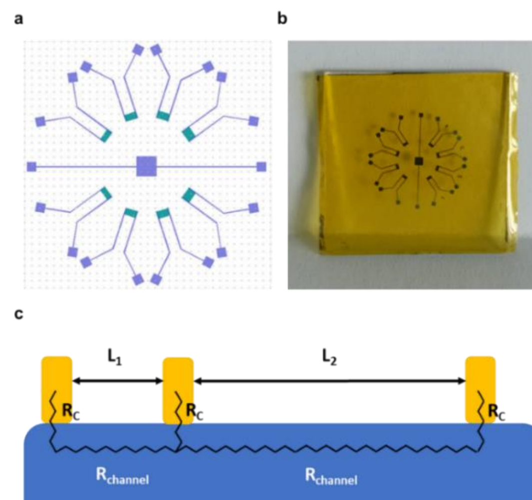

Figure S14. a) CAD design and b) device geometry on flexible PI substrate. c) Schematic of electrical device, where R_T is given by the combination of R_C (*i.e.*, resistance at the metal/semiconductor interface) and $R_{channel}$.

Usually, $R_{channel}$ is defined as $R_{sheet}L/W$, showing a linear dependence on L determined by with uniform physical composition across the channel length L and constant width W, where R_{sheet} is the material sheet resistance in Ω/sq (sq = square).

If we consider $R_{channel}$ as quadratically dependent on L the model equation can be rewritten as Although the expression shows a quadratic dependence on L, the first addend remains unchanged. Therefore, the intercept for $L = 0$ still represents the contact resistance of the system.

Considering

$$R_{channel} = R_{sheet}\frac{L^2}{W} \tag{S12}$$

Equation S11 can be written as

$$R_T = nR_C + \frac{R_{sheet}}{W}L^2 \tag{S13}$$

where, for $L = 0$, we obtain nR_C represented by the x-intercept of the curve fitting in R_T *vs.* L plot, as displayed in **Figure S15**.

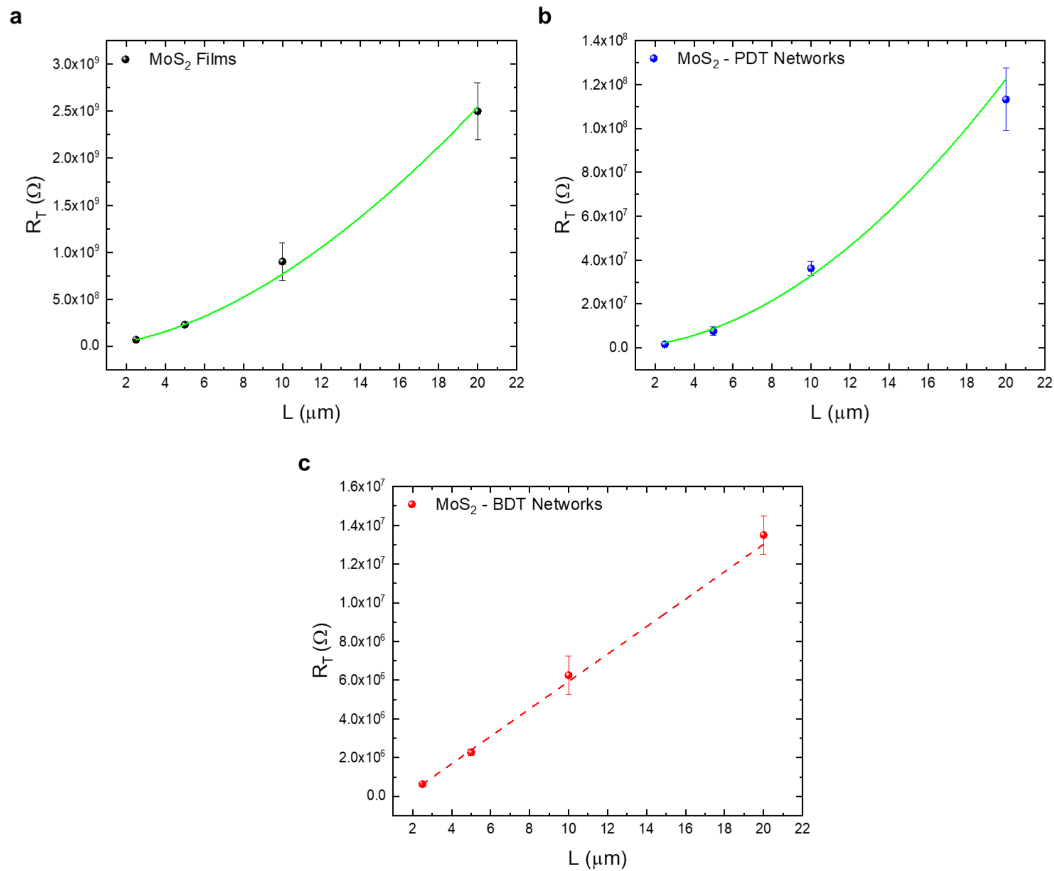

Figure S15. Experimental data reported in R_T *vs.* L plots, as well as allometric and linear fit for a) MoS_2 films, b) MoS_2-PDT networks and c) MoS_2-BDT networks.

	R_C (kΩ)
MoS_2 Films	650 ± 30
MoS_2-PDT Networks	18 ± 9
MoS_2-BDT Networks	3 ± 50

Table S7. R_C values extrapolated from Figure S15 for MoS_2 films, MoS_2-PDT networks and MoS_2-BDT networks.

We observe $R_C << R_T$, therefore, we can rule out its contribution to the overall charge transport.

6. Percolation theory of electrical devices based on MoS_2 films and networks

In the ideal case of 2D materials with uniform physical composition across the channel length L and constant width W, the electrical resistance R is defined as

$$R = \rho \frac{L}{W} = \frac{1}{G} \tag{S14}$$

where $\rho = (1/\sigma)$ and G are the resistivity and conductance, respectively.

Conversely, for highly disordered, defective, and physically non-uniform materials, σ cannot be defined as an intensive quantity and an effective conductivity σ_{eff}, depending on L, must be considered.

The σ *vs*. L behavior found in our devices is shown in **Figure S16**. A $L^{-\beta}$ dependence of σ is highlighted, with $<\beta> = 0.92 \pm 0.05$ close to the theoretical value of 0.95 [19], thereby supporting the percolation analysis derived for MoS_2 films and networks[20–22].

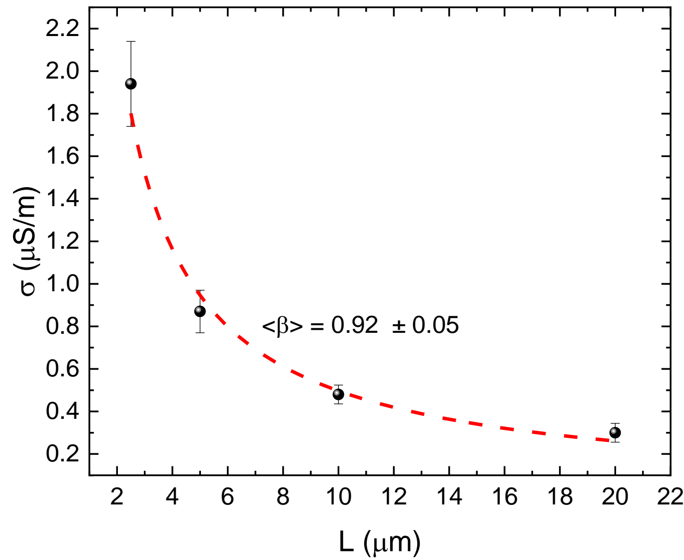

Figure S16. σ *vs*. L plot for MoS_2 films. The β value, extrapolated from the allometric fit, represents the exponent of the percolation theory. The reported value is the mean and standard deviation of 6 devices.

Due to the device fabrication procedure, each value of c_M corresponds inevitably to a different value of k. Therefore, to estimate the contribution to the functionalization, we calculate the ratios between different samples of MoS_2 films

$$r_{k,k'}(L,0,0) = a_{k,k'}(0,0)\, \frac{[p_k(0) - p_c]^t + bL^{-\beta}}{[p_{k'}(0) - p_c]^t + bL^{-\beta}} \tag{S15}$$

The experimental behavior of $r_{k,k'}(L,0,0)$ (**Figure S17**) does not show a clear monotonic dependence on L within errors, meaning that $p_{k'}(0) \sim p_k(0)$. Therefore, although the MoS_2 films have different initial σ (Figure S17), this difference must be interpreted as different values of the average bond conductivity $A_k(0)$.

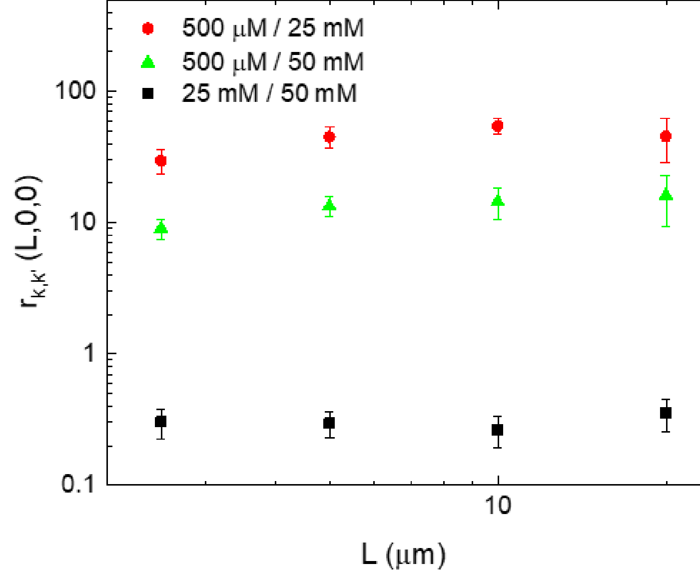

Figure S17. $r_{k,k'}(L,0,0)$ between different MoS_2 films as a function of L.

To explore the effects of the thiol functionalization on the percolation properties of MoS_2 networks, we study the σ dependence on L at three different c_M. Considering

$$r_{k,k}(L, \mathrm{c_M}, 0) \simeq a_{k,k}(\mathrm{c_M}, 0) \frac{[p_k(\mathrm{c_M}) - p_c]^t + bL^{-\beta}}{bL^{-\beta}} \quad \text{(S16)}$$

the experimental determination of $r_{k,k'}(L, c_M, 0)$ for three different values of c_M and the related analytic expressions are reported in the manuscript, while the $a_{k,k}(c_M, 0)$ and $p_k(c_M) - p_C$, obtained by best fit procedure, are shown in **Table S8**.

c_M	$a_{k,k}$	$p_k(c_M) - p_C$
500 µM	1.15	0.054
25 mM	7.58	0.41
50 mM	14.97	0.62

Table S8. Fitted values of the parameters entering Equation S15 at three different c_M.

From Table S8, two effects contribute to increase the electrical conductivity in MoS_2-BDT networks. On one hand, $a_{k,k}(c_M, 0)$ shows the enhancement of already existing percolation paths as a function of c_M. On the other hand, $p_k(c_M) - p_C$ demonstrates the formation of additional paths in MoS_2-BDT networks.

To further corroborate our claim of σ saturation at longer L, we performed σ *vs.* L measurements in the channel length ranging from 2.5 µm to 500 µm. As shown in the **Figure S18**, the saturation regime starts at ~20 µm from where the finite-size effects become negligible.

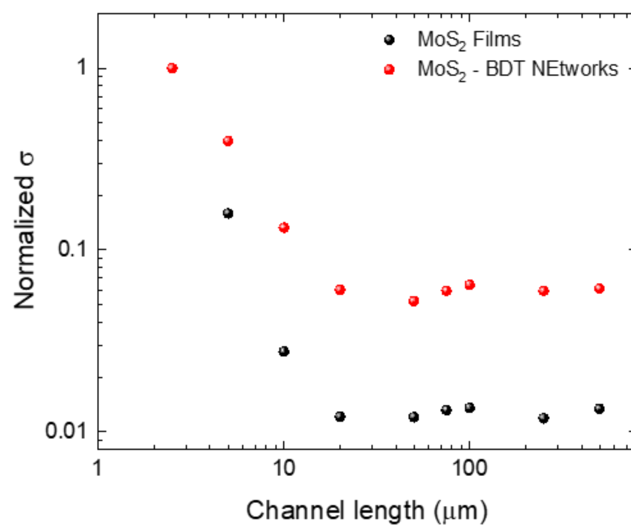

Figure S18. σ *vs.* L plot for MoS_2 films and MoS_2-BDT networks in the range 2.5-500 µm.

7. References

[1] F.-C. Chiu, *Adv. Mater. Sci. Eng.* **2014**, *2014*, 1.
[2] V. K. Sangwan, M. C. Hersam, *Annu. Rev. Phys. Chem.* **2018**, *69*, 299.
[3] N. F. Mott, *Metal-Insulator Transitions*, Taylor & Francis, London, **1990**.
[4] N. F. Mott, E. A. Davis, *Electronic Processes in Non-Crystalline Materials*, Clarendon Press, Oxford, **2012**.
[5] B. I. Shklovskii, A. L. Efros, *Electronic Properties of Doped Semiconductors*, Springer, Berlin, **1984**.
[6] D. Chaudhuri, A. Kumar, R. Nirmala, D. D. Sarma, M. García-Hernández, L. S. S. Chandra, V. Ganesan, *Phys. Rev. B* **2006**, *73*, 075205.
[7] R. Bhatia, K. Kumari, R. Rani, A. Suri, U. Pahuja, D. Singh, *Rev. Phys.* **2018**, *3*, 15.
[8] R. Rosenbaum, R. Haberkern, P. Häussler, E. Palm, T. Murphy, S. Hannahs, B. Brandt, *J. Phys.: Condens. Matter* **2000**, *12*, 9735.
[9] N. Papadopoulos, G. A. Steele, H. S. J. van der Zant, *Phys. Rev. B* **2017**, *96*, 235436.
[10] A. Kovtun, A. Candini, A. Vianelli, A. Boschi, S. Dell'Elce, M. Gobbi, K. H. Kim, S. Lara Avila, P. Samorì, M. Affronte, A. Liscio, V. Palermo, *ACS Nano* **2021**, *15*, 2654.
[11] E. Piatti, A. Arbab, F. Galanti, T. Carey, L. Anzi, D. Spurling, A. Roy, A. Zhussupbekova, K. A. Patel, J. M. Kim, D. Daghero, R. Sordan, V. Nicolosi, R. S. Gonnelli, F. Torrisi, *Nat. Electron.* **2021**, *4*, 893.
[12] J. Xue, S. Huang, J.-Y. Wang, H. Q. Xu, *RSC Adv.* **2019**, *9*, 17885.
[13] H. Abdalla, K. van de Ruit, M. Kemerink, *Sci. Rep.* **2015**, *5*, 16870.
[14] A. G. Kelly, D. O'Suilleabhain, C. Gabbett, J. N. Coleman, *Nat. Rev. Mater.* **2022**, *7*, 217.
[15] S. Ippolito, A. G. Kelly, R. Furlan de Oliveira, M.-A. Stoeckel, D. Iglesias, A. Roy, C. Downing, Z. Bian, L. Lombardi, Y. A. Samad, V. Nicolosi, A. C. Ferrari, J. N. Coleman, P. Samorì, *Nat. Nanotechnol.* **2021**, *16*, 592.
[16] S. M. Sze, K. K. Ng, *Physics of Semiconductor Devices*, John Wiley & Sons, Hoboken, **2006**.
[17] D. K. Schroder, *Semiconductor Material and Device Characterization*, John Wiley & Sons, **2006**.
[18] S. B. Mitta, M. S. Choi, A. Nipane, F. Ali, C. Kim, J. T. Teherani, J. Hone, W. J. Yoo, *2D Mater.* **2021**, *8*, 012002.
[19] B. Derrida, J. Vannimenus, *J. Phys. A: Math. Gen.* **1982**, *15*, L557.
[20] C. H. Seager, G. E. Pike, *Phys. Rev. B* **1974**, *10*, 1435.
[21] A. D. F. Dunbar, J. G. Partridge, M. Schulze, S. Scott, S. A. Brown, in *Proceedings International Conference on MEMS, NANO and Smart Systems*, IEEE Comput. Soc, Canada, **2003**.
[22] B. D. Hughes, in *Encyclopedia of Complexity and Systems Science* (Ed.: R. A. Meyers), Springer, New York, **2009**.